Geophys. J. Int. (20XX) **XXX**, 1–26

Methods and Test Cases for Linking Physics-Based Earthquake and Tsunami Models

E. H. Madden[1,2], M. Bader[3], J. Behrens[4], Y. van Dinther[5,6], A.-A. Gabriel[1], L. Rannabauer[3], T. Ulrich[1], C. Uphoff[3], S. Vater[4], S. Wollherr[1], I. van Zelst[5]

[1] *Department of Earth and Environmental Sciences, Ludwig-Maximilians-Universität München, Munich, Germany*
[2] *Observatório Sismológico, Instituto de Geociências, Universidade de Brasília, Brasília, Brazil*
[3] *Department of Informatics, Technical University of Munich, Garching, Germany*
[4] *Numerical Methods in Geosciences, Department of Mathematics/CEN, Universität Hamburg, Hamburg, Germany*
[5] *Seismology and Wave Physics, Institute of Geophysics, Department of Earth Sciences, ETH Zürich, Zürich, Switzerland*
[6] *Department of Earth Sciences, Utrecht University, Utrecht, The Netherlands*

Received ; in original form

SUMMARY

Despite the inter-dependence of long term deformation, earthquakes and tsunamis, few modelling approaches bridge these processes. To advance the understanding of tsunami generation and earthquake-tsunami interactions, we present new methods for linking physics-based models of subduction zone geodynamics and seismic cycling, three-dimensional dynamic earthquake rupture, and tsunami generation, propagation and inundation. This modeling framework ensures mechanical consistency across temporal and spatial scales. We first present a simplified earthquake-tsunami test case, in which an earthquake rupture occurs on a planar, dipping fault surrounded by a homogeneous material and loaded by a depth-dependent stress field. This is linked to a hydrostatic tsunami model by porting the coseismic seafloor displacements. We detail the applied filters and discuss adequate spatial resolutions for this linkage. We compare tsunamis produced by two earthquake sources that vary by fault strength, and therefore slip, along the top of the fault near the seafloor. The earthquakes exhibit different rupture velocities and slip distributions, while the seafloor displacements and resulting tsunamis are more similar. This demonstrates the utility of linked models to evaluate the effects of certain earthquake characteristics on tsunami behavior. The second test case is more complex, with the initial conditions for the dynamic earthquake rupture scenario taken from a model of long term subduction zone geodynamics and seismic cycling. These conditions include the lithology, stress field, fault geometry, and fault strength, which are physically consistent with one another due to their development together over many slip events in the subduction scenario. Nucleation and rupture propagation occur spontaneously in the linked earthquake scenario. The time-dependent seafloor displacements are used to dynamically source the tsunami. We also compare this dynamically sourced tsunami with a tsunami sourced by the final, static displacements and find that the temporal variation in displacements has a clear influence on the solution. This demonstrates the utility of linked models to isolate the effects of certain modeling choices on the results. In order to encourage widespread use of these test cases, relevant materials are provided publicly. These methods facilitate research into the physical relationships between processes operating across the spatial and temporal time scales of long term deformation, earthquake rupture, and tsunami propagation.

Key words: Earthquake – Tsunami – Geodynamics – Numerical modelling – Subduction – Linkage

1 INTRODUCTION

Subduction zone earthquakes often trigger devastating tsunamis, such as the 2004 Sumatra, 2010 Maule and 2011 Tohoku earthquake-tsunami sequences. In many instances, the wave behavior is not expected, given the earthquake behavior, or tsunamis occur from unexpected sources. A recent example of this is the 28 September 2018 strike-slip earthquake that struck Sulawesi, Indonesia and sourced a tsunami within Palu Bay (Ulrich et al. 2019b). Determining where, when and how tsunamis will occur

demands improved understanding of the physics of earthquake and tsunami interactions.

Numerical modeling provides a unique opportunity to advance knowledge of the physical relationships between long term deformation, earthquakes and tsunamis. However, despite the interdependence of these processes, a modelling approach that bridges them is both geophysically and computationally challenging. Numerous scales in space and time must be captured and resolving the relevant processes is difficult, even in individual models. Here, we review the state-of-the-art modeling approaches that link two of these processes.

Bridging dynamics relevant at both tectonic and seismic cycling timescales through single framework numerical models is achieved by van Dinther et al. (2013b, 2014); Sobolev & Muldashev (2017); Dal Zilio et al. (2018) and van Dinther et al. (2019). Linking separate numerical models is advantageous to traverse spatial and temporal resolutions relevant to tectonics, seismic cycles and dynamic ruptures and to capture physical complexities. Recently, van Zelst et al. (2019) coupled a 2D subduction zone geodynamic and seismic cycle model to a 2D dynamic rupture model, thereby spanning timescales from millions of years to fractions of seconds.

Approaches for linking dynamic earthquake rupture to tsunami models also exist. 2D dynamic rupture simulations are coupled to the time-dependent response of water layers hosting tsunamis by Lotto et al. (2017a,b, 2018). Working with 3D dynamic earthquake rupture models, Ryan et al. (2015) use the final, static seafloor displacements to source a tsunami, while Wendt et al. (2009) use the 3D dynamic displacements. Saito et al. (2019) also use a dynamic, 3D earthquake source to study the influence of seismic waves on a modeled tsunami.

We present two test cases that demonstrate methods to link separate physics-based models, using computational tools that are individually verified. The first test case links a 3D dynamic earthquake rupture model to a tsunami model. While honoring critical parameters and relationships, we keep the model geometry and physics as simple as possible. We present two scenarios: one with slip proceeding to the top of the fault at the seafloor and one with slip restricted to below the surface. The tsunami is sourced by the dynamic seafloor displacements over the entire earthquake phase.

The second test case uses a 2D seismo-thermo-mechanical model of long term subduction and seismic cycles to set the initial conditions for the earthquake model. We follow the methods of van Zelst et al. (2019), but extend the application to a 3D dynamic earthquake rupture. This provides more complex initial conditions for the earthquake model than in the first test case, including a curved fault geometry, heterogeneous stress field and fault strength, and spatially variable material properties. We compare a tsunami sourced by the resulting dynamic seafloor displacements encompassing the entire earthquake phase to a statically-sourced tsunami using the final displacements.

Verification benchmarks exist for dynamic earthquake rupture models (Harris et al. 2009, 2018) and tsunami models (Synolakis et al. 2008), but not for linked modeling. These test cases are the initial steps toward community benchmarks for bridging earthquake and tsunami models. To encourage adoption by others, we detail the physical models and methods used to link the earthquake and tsunami models in Sec. 3 and to link the subduction, earthquake and tsunami models in Sec. 4. We discuss choices and alternatives in Sec. 5. Technical details and information for running the test cases with the computational tools used here are available in the Appendix. We focus on methods here and do not aim to answer all geophysical questions, but we do evaluate these earthquake and tsunami scenarios against observations of events in Sec. 5.

2 MODELLING TOOLS

We aim to use consistent vocabulary throughout the manuscript. A 'computational model' is the computer program discretizing the equations and implementing the numerical workflow. A 'physical model' is the structural setup, governing equations and selected input parameters. A 'scenario' refers to the results achieved by a computational model and according to a specific physical model. We attempt to only use 'model' when the use of the term is unambiguous.

Here, we provide a general overview of the computational models used. The earthquake and tsunami models both are open-source, use unstructured grid discontinuous Galerkin schemes, and are facilitated by highly optimized parallel algorithms and software. An open-source library allows for scalable input of data at several stages of the workflow. The seismo-thermo-mechanical modeling code is an extension of a long-term geodynamic model (Gerya 2011) that also captures individual slip events. It is not open-source.

2.1 Seismo-thermo-mechanical modeling

We use a continuum seismo-thermo-mechanical approach to model both the subduction dynamics relevant on geodynamic time scales and the approximation of earthquake cycle dynamics relevant on seismic cycle time scales (van Dinther et al. 2013a,b, 2014). The computational model is based on a 2D, coupled thermo-mechanical code developed for long-term, geodynamic deformation (Gerya & Yuen 2007). It is extended and validated to simulate earthquake cycles of both analogue (van Dinther et al. 2013a) and natural (e.g., van Dinther et al. 2013b) systems. The numerical method is detailed by van Dinther et al. (2013a,b).

The computational model uses a fully staggered Eulerian, conservative finite difference scheme to implicitly solve the equations for conservation of mass, momentum, and energy in an incompressible medium (Gerya & Yuen 2007). Large deformation and associated advection of stresses and temperature- and stress-dependent material properties are accomplished through a Lagrangian marker-in-cell technique (Gerya & Yuen 2003). Stress and strain are related through visco-elasto-plastic constitutive relations in which a nonlinear Maxwell rheology is combined with a frictional plastic slider. Most material parameters are derived from laboratory experiments (e.g., van Zelst et al. 2019; Gerya & Yuen 2003). Drucker-Prager plasticity includes an invariant, strongly slip rate dependent frictional formulation to simulate spontaneous frictional instabilities (van Dinther et al. 2013a). The slip and stress drop characteristics of these instabilities at spontaneously evolving orientations resemble those of natural earthquakes, albeit at very low slip rates.

2.2 Dynamic earthquake rupture modeling with SeisSol

SeisSol (`http://www.seissol.org`, `https://github.com/SeisSol/SeisSol`) is the computational model used for 3D dynamic earthquake rupture. It solves the seismic wave equation in velocity-stress formulation using an Arbitrary high-order DERivative Discontinuous Galerkin (ADER-DG) scheme. The computational domain is discretized on a tetrahedral mesh (Dumbser &

Käser 2006), which simplifies automatic mesh generation for complicated geometries and facilitates static mesh adaptivity. Fast time to solution within SeisSol is enabled by recent computational optimizations targeting strong scalability on many-core CPUs (Breuer et al. 2014; Heinecke et al. 2014; Rettenberger et al. 2016) and an efficient local time-stepping algorithm (Breuer et al. 2016; Uphoff et al. 2017). SeisSol is verified with several community benchmarks (De La Puente et al. 2009; Pelties et al. 2012, 2014; Wollherr et al. 2018) following the SCEC/USGS Dynamic Rupture Code Verification exercises (Harris et al. 2018).

SeisSol meets cutting edge computational and geophysical challenges. It is used in the largest and longest dynamic rupture model to date (Uphoff et al. 2017). This scenario of the 2004 Sumatra-Andaman earthquake used a 220 million element mesh, order 6 accuracy in space and time, and required 13.9 hours on the entire SuperMUC phase2 supercomputer (86,016 Haswell cores) at the Leibniz Supercomputing Centre in Garching, Germany. SeisSol is specifically suited to solve for rupture propagation along complex, 3D fault geometries. For example, Ulrich et al. (2019a) and Wollherr et al. (2019) capture complex rupture dynamics, including branching and rupture jumps, along the 3D, segmented fault systems ruptured in the 2016 Kaikoura and 1992 Landers earthquakes.

For all SeisSol models, the physical model is built as follows. First, the structure is set using computer-aided design software. This can include topography, bathymetry, material layers, and multiple, non-planar faults. Second, a mesh is generated for this model geometry. Next, the type of seismic source is assigned. Kinematic sources have predetermined fault slip, while slip develops spontaneously for dynamic sources depending on the initial stress state prior to earthquake, the fault geometry, the rock properties and the fault strength. SeisSol employs an elastic or a viscoelastic constitutive law (Käser et al. 2007; Uphoff & Bader 2016) and also can be combined with viscoplastic rheologies (Wollherr et al. 2018). Fault failure follows a laboratory derived frictional failure criterion and slip is controlled by the selected friction law. For example, linear slip-weakening (Ida 1972, 1973; Andrews 1976a), classical rate-and-state (Dieterich 1992; Dunham et al. 2011) and severe velocity-weakening (e.g., Gabriel et al. 2012) friction laws are available.

The physical model is defined by highly flexible configuration files using the Easy Initialization Library (`easi`) (`www.github.com/SeisSol/easi`). `easi` provides several ways to specify how the parameters vary spatially, for example in layers, according to a polynomial configuration, following bi- or trilinear interpolation from a uniform grid, or using a C-like code that is compiled at run-time. The flexibility of `easi` is enhanced by the possibility to combine each component via a function composition.

2.3 Tsunami propagation and inundation modeling with sam(oa)^2

The computational tsunami model is based on the depth-integrated (hydrostatic) shallow water equations. While these are derived under the assumption that vertical velocities are negligible, they efficiently model large scale horizontal flows and wave propagation with high accuracy. The discretization is based on a second-order Runge-Kutta discontinuous Galerkin scheme (Cockburn & Shu 1998; Giraldo & Warburton 2008) on triangular grids and features an accurate and robust wetting and drying scheme for the simulation of flooding and drying events at the coast (Vater & Behrens 2014; Vater et al. 2015, 2019). The scheme is mass-conservative, preserves positivity of the fluid depth and accurately computes small perturbations from the still water state at rest (e.g., tsunami waves). The influence of bathymetry and bottom friction is parameterized through source terms. Adaptive mesh refinement can enable the efficient computation of large domains, while at the same time it allows for high local resolution and geometric accuracy.

This numerical scheme has been recently integrated into the adaptive mesh refinement package sam(oa)^2 (Meister et al. 2016) (`https://gitlab.lrz.de/samoa/samoa`). sam(oa)^2 features efficient adaptive mesh refinement for tree-structured triangular meshes and provides parallelization in shared (using OpenMP) and distributed (via MPI) memory. It has been shown to scale up to thousands of compute cores, with problem sizes that exceed one billion grid cells with dynamic adaptive refinement and coarsening of cells (Meister et al. 2016).

2.4 ASAGI: a pArallel Server for Adaptive GeoInformation

These linked modeling methods require scalable input of data at several stages. For these purposes, we use ASAGI, an open-source library with a simple interface to access Cartesian material and geographic datasets in massively parallel simulations (Rettenberger et al. 2016) (`www.github.com/TUM-I5/ASAGI`). ASAGI organises Cartesian data sets as a collection of tiles. For dynamically adaptive simulations, where parallel partitions may move around in the computational domain, the data tiles are automatically replicated and migrated across compute nodes, if required. In the respective user modes, ASAGI works as a parallel cache, such that the problem to access material or geographic data at a specific location is simplified to a single function call.

3 A TEST CASE FOR LINKING EARTHQUAKE AND TSUNAMI MODELS

This simple test case links 3D dynamic earthquake rupture to tsunami generation, propagation and inundation. The spatial coordinates are kept constant in the earthquake and tsunami models, with the point at $x = 0$, $y = 0$, $z = 0$ bisecting the line where the fault intersects with the earthquake model surface, which is the seafloor in the tsunami model. We present two linked earthquake-tsunami scenarios that differ by the strength of the shallow fault in the earthquake model. To access the materials needed to run this test case, see App. A.

3.1 Dynamic earthquake rupture model and scenario

The earthquake physical model extends from $x = -325$ to 425 km, $y = -375$ to 375 km and $z = -250$ to 0 km. It incorporates a planar fault that is 200 km along strike and extends from the surface to 35 km depth at a 16° dip. The fault intersects the surface. The along-dip length of the fault is 127 km. The model is meshed with a resolution of 400 m element edge lengths on the fault, which ensures accurate resolution of the dynamic processes at the earthquake rupture front. The resolution coarsens away from the fault to an element edge length of 100 km. The resulting mesh consists of 16 mio tetrahedral elements. More details about the mesh are available in App. C1.

The material around the fault is homogeneous with density $\rho = 3775$ kg/m^3, shear modulus $G = 67.5$ GPa and Lame parameter $\lambda = 85.3$ GPa. These values reflect those estimated for oceanic crust in a subduction zone (e.g., Stephenson et al. (2017)),

and so are near the high end of the range for rock types in subduction zones. The pore fluid pressure is depth-dependent and near-lithostatic at $P_f = \rho_f g z$, where $\rho_f = -3000\ kg/m^3$, g is acceleration due to gravity and z is depth (negative below the surface) (Fig. 1a). The three effective principal stresses ($S_1' > S_2' > S_3'$ with compression negative) change linearly with depth, so the effective shear traction, τ_s', and the effective normal traction, τ_n', do as well (Fig.s 1a and 1b).

The fault fails where and when the absolute magnitude of τ_s' meets the fault shear strength:

$$|\tau_s'| = c - \mu_s^{\text{dr}} \tau_n' \tag{1}$$

In addition to τ_n', the fault shear strength is determined from the on-fault cohesion, c, and the apparent static friction coefficient, μ_s^{dr}. The superscript dr refers to the earthquake (dynamic rupture) model and is used for consistency with Sec. 4. We assign a uniform coefficient of apparent static friction, $\mu_s^{\text{dr}} = 0.275$ (Fig. 1c). We compare two earthquake scenarios that differ only by the on-fault cohesion, c. In Scenario A, $c = 0.4$ MPa everywhere below 15 km. Above 15 km depth, c gradually increases to 8 MPa at the top of the fault. In Scenario B, $c = 0.4$ MPa everywhere. Changing c changes the shear strength, as shown in Fig. 1d.

After failure, the fault weakens according to the linear slip weakening friction law (Andrews 1976b) with μ_s^{dr} dropping to $\mu_d^{\text{dr}} = 0.250$ (Fig. 1c) over the slip weakening distance, $D_c = 0.5$ m (Fig. 1e).

In both Scenario A and Scenario B, the earthquake rupture begins by artificial nucleation (forced weakening over time) in a predefined patch in the southeast corner of the fault at 26 km depth. Slip propagates spontaneously outward from this location for approx. 60 s and is stopped at the three buried fault edges (sides and bottom). The high strength near the top of the fault in Scenario A smoothly stops rupture before surface breaking, while slip continues to the surface in Scenario B. Fig. 2 shows the accumulated fault slip and final and maximum vertical surface displacements for both scenarios.

The earthquake in Scenario A has M_w 8.5. The average accumulated slip is 3.8 m and the maximum accumulated slip is 7.6 m. Due to the increase in c near the surface, slip does not reach the seafloor; all fault slip is restricted to below the surface. The rupture velocity is supershear near the nucleation location, but subshear elsewhere. The maximum seafloor uplift over the entire earthquake occurs at 56 s and is 2.6 m. The minimum displacement is -1.0 m and occurs at this same time. The average vertical displacement at this time is 0.6 m. The seafloor displacements continue to change until they reach relatively constant final values at $\sim$ 80 s, with a spatial maximum at this time of 1.9 m, a minimum of -1.0 m and an average of 0.9 m. However, surface waves continue to propagate until the end of the model run at 120 s. The average stress change on the fault is 3.0 MPa, summed from all positive and negative stress changes across the fault.

The earthquake in Scenario B has M_w 8.6. The average accumulated slip is 6.5 m and the maximum accumulated slip is 10.9 m. Fault slip not only reaches the top of the fault, at the seafloor, in this event, but also reaches a maximum value there. Supershear rupture velocity occurs as the rupture proceeds updip from the nucleation location and as the rupture propagates along the top of the fault, but the rupture velocity is subshear along the deeper portion of the fault. As in Scenario A, the maximum and minimum seafloor displacements over the entire earthquake occur around 56 s. They are 3.3 m and -1.1 m, respectively, and the average vertical displacement at this time is 1.2 m. The seafloor displacements reach relatively constant final values at $\sim$ 95 s, with a spatial maximum at this time of 2.6 m, a minimum of -1.2 m and an average value of 0.9 m. In this scenario as well, surface waves continue to propagate until the end of the model run at 124 s. The average stress change on the fault is 3.9 MPa.

3.2 Tsunami propagation and inundation model and scenario

For the tsunami physical model, we choose a simple, synthetic bathymetry set-up to rule out complex effects resulting from a natural seafloor bathymetry and coastal topography. The set-up consists of a flat seafloor above the earthquake source displacement fields and a linearly sloping beach (Fig. 3). Hence, we define the bathymetry by

$$b(x,y) = \begin{cases} 0.05\,(x - x_0) & \text{for } x > x_0 \\ 0 \text{ km} & \text{otherwise,} \end{cases} \tag{2}$$

where $x_0 = 200$ km is the beach toe, where the slope begins. The initial sea surface is flat ('sea-at-rest') and located at $z = 2$ km, which means that the coastline is located at $x = 240$ km. Above this level, the water depth is set to zero. We refer to the sea surface height (ssh) as the deviation from the reference height of 2 km. The size of the domain is from $x = -400$ to 400 km and $y = -400$ to 400 km, which is larger than the horizontal extent of the earthquake physical model in order to minimize model boundary effects. The minimum mesh size is 12.2 m. More details about the mesh are available in App. C2.

We account for temporal variations in the seafloor deformation by adding a perturbation $\Delta b(t,x,y)$ derived from the 3D coseismic seafloor displacements from the earthquake scenario to the initial 2D bathymetry. This is accomplished by the method of Tanioka & Satake (1996), which combines the vertical component of the displacement vector with vertical changes induced by the interaction of horizontal displacement components with bathymetry gradients. The present model includes only a flat seafloor where the displacements arise, so the inclusion of horizontal displacement components has no effect on the tsunami source. However, we include this so that these methods can be used directly for models with realistic, non-trivial bathymetry.

Fig. 3 shows the physical model and the bathymetry perturbation field produced by the Scenario A earthquake at $t = 102$ s. Though it shows only one instance in time, we use the time-dependent seafloor displacements from the entire earthquake scenario. We use the displacements at a resolution of 1000 m. Technical details for this are provided in App. C2.

We apply a temporal filter to the resulting time-dependent bathymetry perturbation field Δb that aims to remove Rayleigh waves present in the earthquake seafloor displacements. We first estimate the frequency range of Rayleigh waves to be higher than 0.006 Hz. We then apply a low-pass filter with a cut-off frequency of 0.0032 Hz. In the resulting filtered bathymetry perturbations, Rayleigh waves are effectively removed, while the displacement signal is essentially untouched. This filtering is further discussed in Sec. 5.1.1 and detailed in App. C2.

During the tsunami, the sea surface reaches a maximal height that matches the maximum seafloor uplift of 2.6 m in Scenario A and 3.3 m in Scenario B. Fig. 4a-c compare cross sections through the sea surface showing the wave profiles from both scenarios at different times. Fig. 4a at $t = 120$ s shows that slip not reaching the seafloor in Scenario A produces a smooth wave, while slip reaching the seafloor in Scenario B initially produces a step-wise

discontinuity. While in reality a step in the sea surface height (ssh) is certainly nonphysical, the nature of a one-layer shallow water approximation imprints the source displacements directly into the water column and thus a step is visible in the tsunami initial state. Fig. 4b shows both waves at $t = 1200$ s, the approximate moment of first inundation. The shape of the waves continues to differ. Near $t = 1600$ s, the Scenario A wave reaches a maximum height at the beach of $ssh = 2.7$ m, while the Scenario B wave reaches $ssh = 3.0$ m (Fig. 4c).

Fig.s 4d and 4e show time series at $x = 240.1$ km (10 km inland from the coast) and $y = -150$ km, $y = 0$ km, or $y = 150$ km, thus tracking the wave height at different locations over time. The highest wave height shown for both Scenario A and Scenario B occurs at $y = 0$ km. The wave heights in both scenarios are asymmetric, with higher waves at $y = 150$ km than at $y = -150$ km. Note that $y = 150$ km corresponds to the part of the coast that is farther from the earthquake hypocenter. This is consistent with the locations of higher fault slip and uplift here in both earthquake scenarios (Fig. 2).

The main characteristics of the inundation for both scenarios are shown in Fig. 5. In both scenarios, the waves reach a maximum runup of 52 m at the center of the beach (near $y = 0$). Away from the center, the runup is smaller. The wave heights are asymmetrical around the center of the beach and are larger toward $y > 0$. In Scenario A, the flooding at the coast ($x = 240$ km) extends across the interval of $y \in [-155.25, 184.5]$ km. This is wider than in Scenario B, in which $y \in [-135, 148.5]$ km is flooded. 40 m inland from the coast, the wave from Scenario A floods a smaller extent, across the interval of $y \in [-47.25, 76.5]$ km, while the wave from Scenario B floods across the interval of $y \in [-54, 87.75]$ km. The wave sourced by the earthquake with fault slip restricted to below the surface in Scenario A inundates a longer stretch of the beach, but a smaller area overall. In contrast, the wave sourced by the earthquake that ruptures all the way to the seafloor in Scenario B inundates a shorter stretch of the beach, but a larger area overall.

4 A TEST CASE FOR LINKING SUBDUCTION, EARTHQUAKE AND TSUNAMI MODELS

We now add complexity by linking a 2D model of geodynamics and seismic cycling capturing long term subduction to the earthquake model, then linking this to a tsunami model. This extends the methods of van Zelst et al. (2019) from 2D to 3D earthquake rupture and creates an earthquake source that is still simplified relative to nature, but includes more complexity than that in the earthquake-tsunami test case. For access to the materials for this test case, see App. A. Technical details are available in App. D.

The three physical models have $x = 0$ in the same location. In the earthquake model, $y = 0$ bisects the fault and runs through the earthquake hypocenter. It is in the same location in the tsunami model, bisecting the seafloor. The surface/seafloor is initially located at $z = 0$ in both the earthquake and tsunami models.

4.1 Long term subduction

4.1.1 Subduction physical model

The physical subduction model is 2D and has an extent of 1500 km in the x-direction by 200 km in the z-direction. The subducting oceanic plate consists of 4 km thick sediments, a 2 km thick basaltic upper crust, a 5 km thick gabbroic lower oceanic crust, and a lithospheric mantle (Fig. 6a). The continental plate consists of a sedimentary wedge, an upper and lower continental crust and a lithospheric mantle layer. A constant velocity of 7.5 cm/yr is applied to the subducting plate to initiate and sustain subduction. Free slip boundary conditions are used at the sides and the top of the model, and there is an open boundary at the bottom. A sticky air approximation is used for the free surface.

The subduction geometry, lithological properties, and temperature develop spontaneously over 4 million years through solving thermo-mechanical conservation equations with a time step of 1000 years (compare Fig.s 6b and 6c). At temperatures below 100°C, materials are velocity strengthening and a transition between 100°C and 150°C leads to velocity weakening at higher temperatures. The down-dip limit of the seismogenic zone develops as viscous deformation becomes progressively more dominant at temperatures above 350°C (van Dinther et al. 2013b). Subsequently, for approximately 30,000 years, the time step is gradually reduced to 5 years to start the seismic cycle phase of the model. The subduction geometry (Fig. 6c) shows the oceanic plate subducting with an average dip of 14.8° above 95 km depth during this phase.

Progressive brittle failure constitutes a slip event in the subduction model and occurs according to Drucker-Prager plasticity. Yielding initiates when the second invariant of the deviatoric stress tensor σ'_{II} (Fig. 6d) meets the yield strength:

$$\sigma'_{II} = C + \mu\Big[1 - (P_f/P)\Big]P \tag{3}$$

Here, C is cohesion, P is the mean pressure, P_f is the pore fluid pressure and μ is the friction coefficient. Note that in the subduction model, there is no differentiation between bulk cohesion of intact rock and on-fault cohesion, c, after failure. Slip behavior after failure is viscoplastic rate dependent, with μ decreasing from its static value μ_s^{sc} to a dynamic value μ_d^{sc}. For consistency with van Zelst et al. (2019), we use the superscript sc to refer to the subduction (seismic cycling) model.

4.1.2 Subduction scenario

Slip events in the subduction scenario are quasi-periodic. They occur mainly in the subduction channel and the accretionary wedge. The events typically nucleate in the basalt, after which they rupture within the sediments in the shallow part of the subduction channel.

We choose one representative slip event for linking. The onset of the slip event is the first time step at which two adjacent points are at failure. Slip initiates at 216–225 km along the fault and proceeds mainly up-dip, where it is stalled in the velocity strengthening region. Slip also arrests down-dip, in the domain dominated by ductile creep. The event exhibits a peak slip of 9.7 m, an average stress drop of 3.9 MPa, and a maximum stress drop of 26.1 MPa. The stress drop is material dependent, with a higher mean stress drop of 10.3 MPa in the basalt and a lower mean stress drop of 1.5 MPa in the sediments.

4.2 Dynamic earthquake rupture

4.2.1 Earthquake physical model

We link long term geodynamics to 3D dynamic rupture by passing the material properties, fault geometry, stress field and frictional parameters for the chosen subduction slip event to the earthquake model. Technical information about how the subduction output is mapped to the earthquake model is in App. D.

The earthquake physical model extends from $x = -800$ to 800 km, $y = -800$ to 800 km and $z = -500$ to 0 km. $x = 0$ is in the same position as $x = 0$ in the section of the subduction model shown in Fig. 6c. The earthquake model domain contains the 3D fault (Fig. 7), for which the geometry must be prescribed. First, fault locations are taken from the subduction slip event every 500 m in the positive x-direction and at the depth of the maximum strain rate over the entire slip event. Then, the 3D fault is built by copying these locations in the positive and negative y-direction (see App. D2). The resulting fault extends along strike from $y = -200$ to 200 km, from $x = 50$ to 373 km and from $z = -6$ to -95 km. It does not intersect the surface. Its dip gradually increases with depth, ranging from 2.3° to 34° and averaging 14.8°.

We mesh this structural model with an on-fault element edge length of 400 m. Away from the fault, the mesh resolution is gradually decreased to a maximum element edge length of 100 km at the model boundaries. Additional mesh information is available in App. D2.

In order to assign 3D properties, we assume that all parameters from the 2D subduction slip event are laterally uniform in the y-direction. The material properties of density, ρ, and shear modulus, G, are taken from the onset of the subduction slip event. The subduction model assumes incompressible rocks with a Poisson's ratio of $\nu = 0.5$. The earthquake model requires compressible materials, so we assign $\nu = 0.25$ and calculate λ, which results in $\lambda = G$. We discuss this further in Sec. 5.1.2.

The effective Cartesian stresses also are mapped to the earthquake model from the onset of the subduction slip event. We use the term effective to indicate the presence of pore fluids. The pore fluid pressure, P_f, is near-lithostatic at all depths (Fig. 8a), as $\gamma = P_f/P = 0.95$ occurs all locations that have fluid present and this is the case along the entire fault in the subduction slip event (van Dinther et al. 2014). The effective normal traction magnitudes are somewhat linearly dependent on depth (Fig. 8a), but the effective shear traction magnitudes reach minima near the surface and deep along the fault, and a maximum near 43 km depth (Fig. 8b).

In the earthquake model, failure occurs according to the frictional criterion in Eq. 1 and is dependent on the effective static coefficient of friction, μ_s^{dr}, on-fault cohesion, c, and the effective normal and shear traction magnitudes. μ_s^{dr} is determined following van Zelst et al. (2019) from the friction in the subduction model at the onset of the slip event, $\mu_{\text{ini}}^{\text{sc}}$, as:

$$\mu_s^{\text{dr}} = \mu_{\text{ini}}^{\text{sc}}(1 - \gamma) = 0.05\mu_{\text{ini}}^{\text{sc}} \tag{4}$$

We use the superscript dr to refer to the earthquake (dynamic rupture) model and the superscript sc to refer to the subduction (seismic cycling) model for consistency with van Zelst et al. (2019). Values for μ_s^{dr} are shown in Fig. 8c. c is set to equal to C from the subduction model (van Zelst et al. 2019) and is shown in Fig. 8d.

After failure, the fault weakens according to the assigned linear slip-weakening friction law. The friction coefficient changes from μ_s^{dr} to an apparent dynamic value, μ_d^{dr}. If the fault location is in a velocity strengthening region of the subduction model, we assign $\mu_d^{\text{dr}} = 0.05\mu_{\text{max}}^{\text{sc}}$, where $\mu_{\text{max}}^{\text{sc}}$ is the maximum friction reached at that location during the entire slip event. This then results in $\mu_d^{\text{dr}} > \mu_s^{\text{dr}}$. If the fault location is in a velocity weakening region, we assign $\mu_d^{\text{dr}} = 0.05\mu_{\text{min}}^{\text{sc}}$, where $\mu_{\text{min}}^{\text{sc}}$ is the minimum value reached at that location during the entire slip event. Values for μ_d^{dr} are shown in Fig. 8c. The decrease from μ_s^{dr} to μ_d^{dr} occurs over the slip weakening distance, D_c. D_c is calculated from the subduction slip event following the methods of van Zelst et al. (2019) and its values are shown in Fig. 8e.

Fig. 9 compares the fault strength and the effective shear traction, τ_s', along a cross-section through the 3D fault in the earthquake model. This reveals that the failure criterion in Eq. 1 is met in three locations initially. These locations are within the shallow sediments, at one additional point at 74.7 km depth, and between 40 and 43 km depth. We prevent failure in the sediments in the earthquake model by setting $c = 5$ MPa here, which is the value of c in the deeper basalt. Note that in the subduction model, velocity strengthening restricts slip here, but this is not invoked in the earthquake model. We also prevent failure at 74.7 km depth by assigning $\mu_s^{\text{dr}} = 0.02$ here.

Between 40 and 43 km depth is where the subduction slip event begins, so we set the nucleation zone here in the earthquake model. This zone is centered at $x = 267$ km, $y = 0$ km, $z = -41.5$ km and has a radius of 1.3 km. As shown in Fig. 8, τ_s' is locally relatively high here. In addition, μ_s^{dr} is locally relatively low, which decreases the fault strength. The minimum value of μ_s^{dr} here is 0.019 and so we ad-hoc set $\mu_s^{\text{dr}} = 0.019$ within the nucleation zone. In order to restrict nucleation laterally, we set $\mu_s^{\text{dr}} = 0.025$ in the region outside of, but at the same depth as, the nucleation zone.

We make one additional adjustment to the earthquake physical model. Near the material contrast at 27 km depth, μ_s^{dr} and μ_d^{dr} are anomalously large (Fig. 8c). We reset the static friction coefficients at the locations of these outliers to the values of material below, such that $\mu_s^{\text{dr}} = 0.025$ and $\mu_s^{\text{dr}} = 0.0097$.

4.2.2 Earthquake scenario

The earthquake begins in the nucleation zone and slips progressively outward in all directions along the fault. In contrast to in the earthquake model from the earthquake-tsunami test case in Sec. 3, this nucleation is not forced, but occurs spontaneously due to the locally high shear traction magnitudes and locally low static frictional strength inherited from the subduction slip event (Fig. 9). This results in a M_w 9.0 earthquake with an average stress change (i.e., dynamic stress drop) of 2.2 MPa. The stress change is calculated from all stress changes (positive and negative) across the fault.

Fault slip does not reach the top of the fault near the surface, but remains restricted to depth. The accumulated slip reaches maxima of 95.5 m in two locations, as shown in Fig. 10a. The average accumulated slip is 42.2 m. As in the subduction slip event, slip along the deep portion of the fault, below the nucleation depth, is restricted. Slip occurs for approximately 150 s, but waves continue to propagate after this. Slow surface waves in the sediments still are visible at the end of the model run at 241 s in Fig. 10b and 10c. This is further discussed at the end of App. D2.1.

The s-wave speed for the basalt around the fault is 3.2 km/s and the rupture velocity in the earthquake scenario exceeds this near the nucleation location and laterally along the fault at the depth of nucleation, where the fault strength is low relative to the local shear traction magnitudes. The majority of the rupture occurs at sub-shear speeds, however.

The maximum vertical surface displacement after the earthquake is complete (at 241 s) is 15.7 m, the minimum is -6.7 m (Fig.s 10b and 10c), and the average is 3.3 m. However, the maximum uplift over the entire earthquake is 28.1 m and occurs at 100 s (Fig. 11). At this time, the minimum vertical displacement is -5.6 m and the average is 3.6 m.

4.3 Tsunami propagation and inundation

4.3.1 Tsunami physical model

The set-up for the tsunami model is the same as that described for the earthquake-tsunami test case in Sec. 3.2, except that the beach toe, where the slope begins, is located at $x_0 = 500$ km (Fig. 11), the coast is located at $x = 540$ km, and the size of the domain is from $x = -600$ to 600 km and $y = -600$ to 600 km. Again, we use the time-dependent 3D seafloor displacements from the earthquake scenario to compute a bathymetry perturbation $\Delta b(t, x, y)$, which is the source for the initial wave generation in the tsunami model. In contrast to the earthquake-tsunami test case, the displacements here are symmetrical about the x-axis during the entire earthquake (Fig.s 10c and 11). We use the displacements at a resolution of 1000 m and technical details regarding this are in App. D3.

For the temporal filtering to remove Rayleigh waves, we estimate their displacement spectrum to carry non-negligible energy at frequencies above 0.016 Hz. To not significantly alter the longer-period displacement signal close to the center of the earthquake, the cutoff frequency of the low-pass filter is set to 0.0155 Hz. In contrast to Sec. 3.2, this damps the Rayleigh waves by only ≈ 62 %. The non-trivial choice of filtering with respect to surface waves is further discussed in Sec. 5.1.1 and D3.

4.3.2 Tsunami scenario

Three cross sections through the sea surface along $y = 0$ at different moments in time are shown in Fig. 12. The sea surface height (ssh) initially reflects the vertical displacement magnitudes from earthquake (Fig. 12a). The tsunami then develops a circular wave propagating away from the source. The wave arrives at the coast (located at $x = 540$ km) at ~ 2050 s (Fig. 12b). Wave height reaches a maximum of $ssh = 23$ m at 2450 s (Fig. 12c).

Fig. 13 shows the history of inundation. Inundation is symmetric around the center of the coast at $y = 0$ km. The coast between $y \in [-414.0, 414.0]$ km is inundated after 3100 s. At 281 m away from the coast, only areas in the interval $y \in [-126.0, 126.0]$ km are flooded. The maximum runup length is 527 m, which is reached after 2310 s.

5 DISCUSSION

5.1 Linking methods: choices and alternatives

In developing these methods for linking subduction, earthquake and tsunami models, we have made several decisions about how to handle the linkage across space and time. We also have simplified the physical models relative to the capabilities of the computational models used. We discuss these choices and alternatives here.

5.1.1 Earthquake-tsunami linkage: temporal filtering

How to handle seismic surface waves in the tsunami source depends both the modeling choices and the scenario. In terms of modeling choices, we note that it is the hydrostatic approach of the tsunami computational model used here that requires consideration of filtering. The seafloor displacement fields produced by the earthquake model include seismic surface waves (aka Rayleigh waves) that disturb the tsunami model, due to the fact that shallow water theory cannot account for such fast waves. When a fast seismic wave is used in the time dependent bathymetry perturbation, Δb, it excites the water column from below much faster than any tsunami wave can travel and causes an artificial signal. In reality, these seismic waves transform into acoustic or other high-frequency waves that are quickly dissipated in the water column and do not contribute significantly to the hydrodynamic sea surface displacement. However, we must consider them in this modeling framework. For a contrasting example, Lotto et al. (2018) use a 2D, full-physics approach that couples dynamic earthquake rupture, the acoustic ocean response and the tsunami wavefield in one self-consistent framework. This does not require any additional consideration of the seismic surface waves. In terms of how the scenario influences the need for filtering, we point to recent work by Saito et al. (2019), which finds that when the high-frequency content of seismic waves is limited, it has little influence on low-frequency sea surface displacement.

We choose to damp the high-frequency components in the bathymetry perturbation in the methods we present here in order to avoid any possible non-physical effects and to widen the applicability of these methods to many scenarios. We choose a low-pass filter that damps the fast traveling seismic surface waves, while leaving the longer period displacement signal at the center of the earthquake displacement field untouched. Since the computed frequencies for the gravity waves (i.e. the relevant tsunami waves) are below 0.0015 Hz, we are confident that the filtering does not remove any signals important for the tsunami. Low-pass filters of high order provide a viable option, as they allow a high magnitude descent after the cutoff frequency. However, as shown in Sec. 4.3, this approach does not always lead to a complete removal of fast seismic surface waves. Other scenarios might require the development of more sophisticated methods.

5.1.2 Subduction-earthquake linkage: porting the material, yield and slip conditions

The subduction model is 2D and the earthquake model is 3D, which presents numerous possibilities for mapping conditions from the subduction slip event to the earthquake model. By assuming that the fault, material properties and all linked on-fault conditions are constant in the y-direction, we choose a technically simple approach. This provides a straight-forward presentation of model linkage, but likely does not reflect subduction zone characteristics.

Another significant decision is in assigning Poisson's ratio, ν, in the earthquake model. The subduction model assumes incompressible rock with $\nu = 0.5$, which is valid over long time frames, but not appropriate for dynamic earthquake rupture modeling. We choose $\nu = 0.25$. Keeping all other parameters constant, van Zelst et al. (2019) find that, when linking a subduction slip event to a 2D earthquake model, using a larger ν results in less fault slip during the earthquake. Therefore, increasing ν is one way to decrease slip magnitudes in a subduction-linked earthquake scenario. Material dependence of ν could also be considered.

Yielding is governed by different processes in the subduction and earthquake models. The subduction model employs Drucker-Prager plastic yielding to capture the brittle failure of intact rock (Eq. 3), while the earthquake model follows a laboratory-derived criterion for frictional failure along a pre-existing surface (Eq. 1). The linking methods presented here assume that the two yield criteria can be governed by the same initial conditions. This is expressed by Eq. 4, which relates the static coefficients of friction in the subduction and earthquake models and results from equating the two yield criteria and solving (van Zelst et al. 2019). This assumption

is valid down to at least 55 km depth and is reasonable up to 95 km depth (van Zelst et al. 2019). Following these methods, we see progressive slip in the subduction slip event and spontaneous nucleation, propagation and arrest in the linked 3D earthquake scenario.

Processes after yielding also differ in the subduction and earthquake models. To link these conditions, we set the dynamic friction coefficient in the earthquake model to the maximum or minimum friction reached during the subduction slip event, depending on whether the location is in a velocity strengthening or velocity weakening region, respectively. The distance over which weakening occurs, D_c, is constrained such that the friction drop is the same in the subduction and earthquake models (van Zelst et al. 2019). However, the peak slip magnitudes in the earthquake scenario are much higher than those in the subduction slip event and may be unrealistic. In contrast, the average stress drops are similar in the subduction slip event and the earthquake scenario. Thus, alternative methods for linking the models after yielding must be considered carefully.

5.1.3 Modeling capabilities

Both test cases are simplified relative to nature and the capabilities of the employed computational models. We restrict the constitutive behavior of all earthquake models to purely elastic and employ a simple linear slip weakening friction law, though SeisSol provides alternatives. We also exclude complex topography and bathymetry, though realistic representations are permissible in all three computational models. In addition, we account for bathymetry's influence on the seafloor displacements in the methods for linking the earthquake and tsunami models, so no modifications to the methods are required to incorporate bathymetry and topography. We look forward to developing additional test cases in the future that take advantage of the more complex capabilities of these and other computational models.

A few studies use more complex applications of these computational models. van Zelst et al. (2019) incorporate the subduction zone topography into a linked, 2D earthquake model and underscore the importance of using material dependent stresses and frictional properties that develop during long term subduction to accurately produce the seismic wavefield in linked 2D earthquake scenarios. Wollherr et al. (2018) present similar 2D linked models, but focus on the influence of plastic off-fault deformation in the earthquake models. Ulrich et al. (2019b) incorporate strongly rate-weakening friction and off-fault plasticity into a model of the 2018 strike-slip Sulawesi earthquake. By coupling the results to a tsunami model honoring complex bathymetry within Palu Bay, where a subsequent tsunami occurred, Ulrich et al. (2019b) produce a tsunami scenario that matches the available data. These studies highlight the geophysical insights facilitated by linked modeling approaches.

5.2 Utility of linked modeling approaches

These methods to link subduction, earthquake and tsunami models facilitate research on the ways we study tsunami genesis and the physical relationships between processes operating across the spatial and temporal scales of long term deformation, earthquake rupture and tsunami propagation. We demonstrate that these methods permit further study of when and where modeling choices influence results by comparing the dynamically-sourced tsunami from the subduction-earthquake-tsunami test case to a statically-sourced tsunami. We demonstrate that these methods permit further study of how certain initial model conditions influence the results by comparing the two scenarios from the earthquake-tsunami test case.

5.2.1 Static vs. dynamic tsunami sources

The earthquake in the subduction-earthquake-tsunami test case yields high variation of the seafloor displacement in time (Fig. 14). We thus choose the tsunami scenario from this test case in this analysis of the differences that result from using a dynamic versus a static source.

We use the filtered bathymetry perturbation, $\Delta b(t, x, y)$, at the end of the earthquake scenario as a static tsunami source. We shift the simulation time by 380 s compared to the dynamically sourced tsunami, in order to synchronize the scenarios to the time when the coast is first inundated. This allows for a better comparison of the waves on a temporal scale. Note that the maximum seafloor uplift is 16.6 m after the earthquake is complete (Fig. 10b), but that the maximum uplift during the entire earthquake is 29.1 m and occurs at 100 s (Fig. 11).

Fig. 14 shows a comparison of the sea surface height (ssh) along two cross sections for waves from both sources at $t = 420$ s. The general pattern of the wave is similar for both sources, but ssh differs locally. In the cross-section at $y = 0$, the peak of the statically sourced wave is 1.1 m higher than the dynamically sourced wave at that location. Along the line at $y = 150$ km, it is 1.3 m lower. Differences increase away from the wave peaks. This shows how the different sources can affect the spatial distribution of the tsunami waves.

Temporal differences between the statically and dynamically sourced waves are large near the center of the coast, but not everywhere. Fig. 15 shows time series of ssh near the coast at $x = 540$ km and at $y = 0$ km and $y = 150$ km. Clearly visible is the larger wave in the case of the static source at $y = 0$ km. However, the wave behaviors over time are similar at $y = 150$ km.

Fig. 16 shows the spatial distribution of the difference in temporal maxima of inundation depth between the dynamic and the static source. In agreement with the ssh time series near the coast, we see that the static source causes a higher inundation depth, by up to 2.3 m, at the center of the beach. Farther from the center, the differences are less and the inundation depth of the dynamically sourced wave is larger, by up to 0.6 m, than that of the statically sourced wave.

We conclude that results from a static versus a dynamic tsunami source may differ when the seafloor displacement field varies through space and time. This strongly depends on the nature and extent of the earthquake scenario. We present this analysis to demonstrate how the earthquake-tsunami linking methods facilitate such comparisons and can help determine when different modeling approaches are most appropriate.

5.2.2 Influence of fault slip near the seafloor

We now compare the two scenarios in the earthquake-tsunami test case in order to show the usefulness of these models to isolate the influence of certain source characteristics. In comparing the earthquakes and tsunamis, we focus on slip, displacement and wave height characteristics and do not analyse the scenarios in terms of other macroscopic earthquake and tsunami behavior (e.g. rupture speed, seismic radiation efficiency, tsunami velocity), as this test case does not provide enough information to do so satisfactorily. Several of these other characteristics are discussed in Sec. 5.3.

The higher strength along the top of the fault in the earthquake model for Scenario A prohibits slip to the surface, while a maximum slip value is reached at the top of the fault in Scenario B. Maximum accumulated slip reaches 7.6 m and 10.9 m in Scenarios A and B, respectively, while average slip is 3.8 m in Scenario A and 6.5 m in Scenario B. This large difference is notable, as earthquakes are often characterized by their average slip.

For these scenarios, the large difference in slip magnitudes and distributions on the fault, even near the seafloor, do not result in large differences in the vertical displacements or tsunami heights. Maximum uplift is 2.6 m in Scenario A and 3.3 m in Scenario B and these maxima occur at 56 s (Fig. 2b and Fig. 2e). The maximum wave heights for the resulting tsunamis match these displacements, and so differ by 0.7 m. When the tsunami waves along $y = -54.8$ km arrive at the coast, the difference in the wave heights is 0.3 m (Fig. 4c). The Scenario A tsunami inundates a longer stretch of the coast, but a smaller area overall, while the Scenario B tsunami inundates a shorter stretch of the coast, but a larger area overall (Fig. 5). However, the waves have the same runup distance of 52.0 m from the coast and inundate at similar rates.

Given that data collected for tsunamis is typically disparate, it is likely that it would not be possible to observationally distinguish between these two tsunamis. It follows that the data constraints might not be robust enough to choose between these two possible earthquake sources. At the same time, it is possible that the noted variations in wave heights and indundation patterns, though small, directly relate to the variation in slip accumulated at the top of the fault where it intersects the surface and the resulting seafloor displacements in these two scenarios. These earthquake models and methods can be adjusted to test the influence of this earthquake characteristic (i.e. slip to the trench) more rigorously.

5.3 Realistic scenarios?

While the primary focus of this work is on linking methods, here we put the linked models into context by comparing them against observed events. For the earthquake-tsunami test cases, in general, the Scenario A earthquake is more realistic than the Scenario B earthquake. However, both earthquake scenarios produce tsunamis that are realistic when compared to data. Both the earthquake and tsunami scenarios from the subduction-earthquake-tsunami test case exhibit some unrealistic characteristics, though comparison against data is challenging.

5.3.1 Earthquake-tsunami test case scenarios

Based on their magnitudes (M_w 8.5–8.6), fault area (125 km by 200 km), and slip distributions, the two earthquakes scenarios in the earthquake-tsunami test case are comparable to tsunami-generating subduction zone events such as the M_w 8.5 Bengkulu earthquake that occurred off the southwestern coast of Sumatra in 2007 (Gusman et al. 2010; Seno 2014) and the M_w 8.5 South Peru earthquake that occurred in 2001 (Pritchard et al. 2007; Seno 2014). The Bengkulu earthquake had slip restricted to below 10 km depth, with most slip occurring at 16–40 km depth and reaching a maximum of 6–7 m (Gusman et al. 2010). The slip distribution and maximum slip in the Scenario A earthquake are consistent with this event. In the 2001 South Peru earthquake, high slip may have occurred at shallower (5–10 km) depths, though whether or not slip occurred at the trench is inconclusive (Pritchard et al. 2007). The slip distribution in the Scenario B earthquake is similar to this. However, slip in this scenario reaches maxima of 10.9 m, including at the trench, versus the 6 m maximum reported for the South Peru event (Pritchard et al. 2007).

Subduction zone earthquakes typically exhibit sub-shear rupture speeds on average. The Scenario A earthquake exhibits localised supershear rupture velocity near the hypocenter, but not elsewhere. Such localized supershear episodes may occur in nature, but are difficult to resolve. The Scenario B earthquake exhibits supershear velocities near the hypocenter and also along the fault where it intersects with the surface, which has not been observed for subduction zone earthquakes. So, the very low strength on the top of the fault near the seafloor in this model allows unrealistic rupture speeds to occur. It is typical in dynamic rupture models to increase cohesion (or assign velocity-strengthening behavior) close to the surface to prevent supershear rupture velocity. However, this can have the consequence of prohibiting some types of recently observed near-surface behavior, such as the large slip near the trench in the 2011 Tohoku earthquake (Wei et al. 2012). We are unable to adequately explore this complexity here, but aim to provide simple examples through these test cases that illuminate basic differences in rupture behaviour and the related effects on tsunami genesis. We point out that these models are readily extendable to more complex and realistic parametrisations, to address the very issues raised here or others related to earthquake-tsunami behaviors and interactions.

We also compare the resulting tsunami scenarios to data recorded for the tsunami following the 2001 South Peru earthquake. This earthquake produced a tsunami with peak-to-trough maximum wave heights of 1.0–2.5 m at three different tide stations (USGS 2019). This is similar to the tsunami results in both Scenarios A and B, which have maximum wave heights equal to the maximum displacements of 2.6 m and 3.3 m, respectively, that then decrease over time until the waves reach the coast. It is of note that the Scenario B earthquake may not be dynamically realistic, but sources a reasonable tsunami, at least when compared against sparse data. As discussed in Sec. 5.2.2, observational tsunami data may not be able to distinguish between these two tsunamis or the discriminate between these two possible sources.

5.3.2 Subduction-earthquake-tsunami test case scenarios

The earthquake from the subduction-earthquake-tsunami test case is a M_w 9.0 event. This magnitude and the model fault dimensions are similar to those for the M_w 9.0 Tohoku megathrust earthquake that occurred in 2011. The largest difference is that slip is restricted along the shallow fault near the surface in the scenario, while the near-surface part of the megathrust fault likely slipped during the Tohoku earthquake (Sun et al. 2017). We note that this is influenced by the linkage methods, in which we impose a higher cohesion in the sediments near the surface in the earthquake model, where rate-dependent velocity-strengthening is permitted in the subduction model (Sec. 4.2.1). Otherwise, a rupture front develops here in the earthquake scenario.

The average accumulated slip in the earthquake scenario is 42.2 m and the maximum is 95.5 m and occurs in two separate locations on the fault (Fig. 10a). This maximum slip is high relative to many estimates from slip inversions for the Tohoku earthquake, but is similar to the highest maximum values out of a compilation of inversion models (Sun et al. 2017). While this comparison is limited, given that maximum fault slip is hard to resolve by inversion due to restrictions in resolution and uniqueness, and is not available observationally, this scenario may be modified by the interested modeler to yield lower on-fault slip. For example, magnitudes of

the shear moduli in the subduction model are on the low end of inferred values, and are therefore low in the earthquake model as well, which generally increases fault slip. Also, the methods by which the material properties are linked from the subduction to the earthquake model also influences slip, as discussed in Sec. 5.1.2. Finally, smaller slip maxima may be achieved by earthquake models that account for non-smooth fault geometry in the trench parallel direction, off-fault plasticity, and/or more complex on-fault friction laws.

The rupture speed of this earthquake varies along the fault, but averages ~ 2.1 km/s. This is sub-shear relative to the s-wave speed in the basalt around the model fault (3.2 km/s) and similar to the 2.5 km/s mean rupture speed estimated for the Tohoku earthquake (after 80 s) by Ammon et al. (2011). Supershear rupture velocities occur locally near the hypocenter and in isolated regions along the fault at the depth of nucleation, where the fault strength is low relative to the local shear traction magnitudes. As discussed in Sec. 5.2.2, local occurrences of supershear may be realistic, but are challenging to resolve observationally. This makes it difficult to evaluate how realistic the scenario is in this sense.

The vertical seafloor displacements from the Tohoku earthquake are estimated to be ~ 10 m at the trench (Fujiwara et al. 2011). The maximum uplift produced in this earthquake scenario is away from the trench and is 28.1 m, while the average vertical displacement at this time is 3.6 m. The tsunami sourced by this earthquake scenario reaches a peak-to-trough height of ~ 15 m (Fig. 15), which also is large when compared to estimates for the tsunami that followed the Tohoku earthquake. A maximum value of 6.8 m was reached at Iwate Kamaishi-oki, while heights of 6 m were reached at several other locations (Japan Meteorological Agency 2019). Though this comparison is difficult, due to the complex interplay of bathymetry, sea surface height, and wave travel time, it seems likely that the maximum uplift and the height of the tsunami wave in this earthquake scenario are high. Suggestions for decreasing uplift during this earthquake scenario include those previously suggested for decreasing fault slip.

5.4 Toward community benchmarks

Community benchmarks exist for dynamic earthquake rupture models alone and for tsunami models alone, but not for linked models. The here presented test cases form a basis for community verification benchmarks of linked modeling. Toward this goal, they are kept as simple as possible and most of the tools used to build and run the models are open-source. Information about access to model input and output files, scripts and meshes is available in App. A. Where to find the computational models is included in App. B. Technical details for building and running the models are provided in App.s C and D.

6 CONCLUSIONS

Past earthquake-tsunami sequences have been surprising, with devastating consequences, motivating a better understanding of the physical connections between tectonics, earthquake dynamics and tsunami genesis. Linked modeling approaches that ensure mechanical consistency in physical parameters across temporal and spatial scales are ideally suited to such research. We present methods for linking subduction, earthquake rupture and tsunami models in the form of two test cases. We do not aim to answer all geophysical questions raised by these test cases, but to present methods for linkage, demonstrate the utility of linked modeling, and facilitate discussion of best practices.

The earthquake-tsunami test case is highly simplified, making it well-suited for reproduction by others using alternative computational tools or linked modeling approaches. We also use this test case to demonstrate the utility of linked models to isolate the influence of a single parameter on earthquake and tsunami behavior. We compare two earthquake sources: one with high strength at the top of the fault and one with low strength. The former yields a buried rupture, while the latter allows slip to occur all the way to the seafloor and has localized high slip magnitudes and rupture velocity. The different earthquake sources produce tsunamis that differ in terms of runup patterns, but are indistinguishable in many other aspects.

The subduction-earthquake-tsunami test case presents methods for linking geodynamically constrained seismic cycling, 3D dynamic earthquake rupture, and tsunami propagation and inundation. This test case is aimed at understanding how long term and short term processes relate, and how to best link these processes across numerical models. To assess the influence of modeling approaches on tsunami results, we compare a dynamically-sourced tsunami with a tsunami produced by static displacements only. The two sets of modeled waves are distinct, suggesting that the temporal variation of seafloor displacements should not be ignored when modeling tsunamis sourced by complex, long-lived earthquakes. However, the influence of the displacement dynamics varies through time and begs further study.

7 ACKNOWLEDGEMENTS

This effort has and continues to require intense cross-disciplinary collaboration and we want to acknowledge the strong team effort that has made it possible. In addition to the authors, a wide group has contributed to this effort. First, we would like to thank the Volkswagen Foundation (VolkswagenStiftung) for extended funding and excellent support of the ASCETE and ASCETE II projects (`www.ascete.de`). Second, we want to recognize the following researchers that have contributed directly to this project over its years in development: N. Beisiegel, A. Breuer, L. Dalguer, A. Fichtner, P. Galvez, H. Igel, A. Jeschke, M. Käser, O. Meister, C. Pelties, K. Rahnema and S. Rettenberger.

Finally, participants in the 1st and 2nd ASCETE Workshops on Coupling Earthquakes and Tsunamis held in Sudelfeld Bayrischzell, Germany provided motivation for the development of these test cases and feedback on their design. We look forward to continuing discussions with the earthquake and tsunami modeling communities.

Computing resources were provided by the Institute of Geophysics of LMU Munich (Oeser et al. 2006), the Leibniz Supercomputing Centre (LRZ, projects no. h019z, pr63qo and pr45fi on SuperMUC), the Center for Earth System Research and Sustainability (CEN) at University of Hamburg, and the Swiss National Supercomputing Center (project no. s741).

E.H.M., T.U., S.W. and A.-A.G. acknowledge additional support by the German Research Foundation (DFG) (projects no. KA 2281/4-1, GA 2465/2-1, GA 2465/3-1), by BaCaTec (project no. A4) and BayLat, by KONWIHR – the Bavarian Competence Network for Technical and Scientific High Performance Computing (project NewWave), by KAUST-CRG (GAST, grant no. ORS-2016-CRG5-3027 and FRAGEN, grant no. ORS-2017-CRG6 3389.02), by the European Union's Horizon 2020 re-

search and innovation program (ExaHyPE, grant no. 671698 and ChEESE, grant no. 823844).

REFERENCES

Ammon, C. J., Lay, T., Kanamori, H., & Cleveland, M., 2011. A rupture model of the 2011 off the Pacific coast of Tohoku Earthquake, *Earth, Planets and Space*, **63**(7), 693–696.

Andrews, D. J., 1976a. Rupture propagation with finite stress in antiplane strain, *Journal of Geophysical Research*, **81**(20), 3575–3582.

Andrews, D. J., 1976b. RUPTURE VELOCITY OF PLANE STRAIN SHEAR CRACKS., *J Geophys Res*, **81**(32), 5679–5687.

Breuer, A., Heinecke, A., Rettenberger, S., Bader, M., Gabriel, A.-A., & Pelties, C., 2014. Sustained Petascale Performance of Seismic Simulations with SeisSol on SuperMUC, in *Supercomputing. ISC 2014. Lecture Notes in Computer Science, vol 8488*, pp. 1–18, eds Kunkel J.M., Ludwig T., & Meuer H.W., Springer, Cham.

Breuer, A., Heinecke, A., & Bader, M., 2016. Petascale local time stepping for the ader-dg finite element method, in *2016 IEEE International Parallel & Distributed Processing Symposium*, pp. 854–863.

Cockburn, B. & Shu, C.-W., 1998. The Runge-Kutta discontinuous Galerkin method for conservation laws V: Multidimensional systems, *Journal of Computational Physics*, **141**(2), 199–224.

Dal Zilio, L., van Dinther, Y., Gerya, T., & Pranger, C., 2018. Seismic behaviour of mountain belts controlled by plate convergence rate, *Earth and Planetary Science Letters*, **482**, 81–92.

Day, S. M., Dalguer, L. A., Lapusta, N., & Liu, Y., 2005. Comparison of finite difference and boundary integral solutions to three-dimensional spontaneous rupture, *Journal of Geophysical Research: Solid Earth*, **110**(B12307).

De La Puente, J., Ampuero, J. P., & Käser, M., 2009. Dynamic rupture modeling on unstructured meshes using a discontinuous Galerkin method, *Journal of Geophysical Research: Solid Earth*, **114**(10), 1–17.

Dieterich, J. H., 1992. Earthquake nucleation on faults with rate-and state-dependent strength, *Tectonophysics*, **211**(1-4), 115–134.

Dumbser, M. & Käser, M., 2006. An arbitrary high-order discontinuous Galerkin method for elastic waves on unstructured meshes - II. The three-dimensional isotropic case, *Geophysical Journal International*, **167**(1), 319–336.

Dunham, E. M., Belanger, D., Cong, L., & Kozdon, J. E., 2011. Earthquake Ruptures with Strongly Rate-Weakening Friction and Off-Fault Plasticity, Part 1: Planar Faults, *Bulletin of the Seismological Society of America*, **101**(5), 2296–2307.

Fujiwara, T., Kodaira, S., No, T., Kaiho, Y., Takahashi, N., & Kaneda, Y., 2011. The 2011 Tohoku-Oki Earthquake: Displacement Reaching the Trench Axis, *Science*, **334**(6060), 1240.

Gabriel, A.-A., Ampuero, J. P., Dalguer, L. A., & Mai, P. M., 2012. The transition of dynamic rupture styles in elastic media under velocity-weakening friction, *Journal of Geophysical Research: Solid Earth*, **117**(9), 1–20.

Gerya, T., 2011. Future directions in subduction modeling, *Journal of Geodynamics*, **52**(5), 344–378.

Gerya, T. V. & Yuen, D. A., 2003. Characteristics-based marker-in-cell method with conservative finite-differences schemes for modeling geological flows with strongly variable transport properties, *Physics of the Earth and Planetary Interiors*, **140**(4), 293–318.

Gerya, T. V. & Yuen, D. A., 2007. Robust characteristics method for modelling multiphase visco-elasto-plastic thermo-mechanical problems, *Physics of the Earth and Planetary Interiors*, **163**, 83–105.

Geuzaine, C. & Remacle, J.-F., 2009. Gmsh: A 3-D finite element mesh generator with built-in pre- and post-processing facilities, *International Journal for Numerical Methods in Engineering*, **79**(11), 1309–1331.

Giraldo, F. X. & Warburton, T., 2008. A high-order triangular discontinuous galerkin oceanic shallow water model, *International Journal for Numerical Methods in Fluids*, **56**(7), 899–925.

Gusman, A., Tanioka, Y., Kobayashi, T., Latief, H., & Pandoe, W., 2010. Slip distribution of the 2007 Bengkulu earthquake inferred from tsunami waveforms and InSAR data, *J. Geophys. Res*, **115**.

Harris, R. A., Barall, M., Archuleta, R., Dunham, E., Aagaard, B., Ampuero, J. P., Bhat, H., Cruz-Atienza, V., Dalguer, L., Dawson, P., Day, S., Duan, B., Ely, G., Kaneko, Y., Kase, Y., Lapusta, N., Liu, Y., Ma, S., Oglesby, D., Olsen, K., Pitarka, A., Song, S., & Templeton, E., 2009. The SCEC/USGS Dynamic Earthquake Rupture Code Verification Exercise, *Seismological Research Letters*, **80**(1), 119–126.

Harris, R. A., Barall, M., Aagaard, B., Ma, S., Roten, D., Olsen, K., Duan, B., Liu, D., Luo, B., Bai, K., Ampuero, J.-P., Kaneko, Y., Gabriel, A.-A., Duru, K., Ulrich, T., Wollherr, S., Shi, Z., Dunham, E., Bydlon, S., Zhang, Z., Chen, X., Somala, S. N., Pelties, C., Tago, J., Cruz-Atienza, V. M., Kozdon, J., Daub, E., Aslam, K., Kase, Y., Withers, K., & Dalguer, L., 2018. A Suite of Exercises for Verifying Dynamic Earthquake Rupture Codes, *Seismological Research Letters*, **89**(3), 1146–1162.

Heinecke, A., Breuer, A., Rettenberger, S., Bader, M., Gabriel, A. A., Pelties, C., Bode, A., Barth, W., Liao, X. K., Vaidyanathan, K., Smelyanskiy, M., & Dubey, P., 2014. Petascale High Order Dynamic Rupture Earthquake Simulations on Heterogeneous Supercomputers, in *International Conference for High Performance Computing, Networking, Storage and Analysis, SC*.

Ida, Y., 1972. Cohesive force across the tip of a longitudinal-shear crack and Griffith's specific surface energy, *Journal of Geophysical Research*, **77**(20), 3796–3805.

Ida, Y., 1973. Stress concentration and unsteady propagation of longitudinal shear cracks, *Journal of Geophysical Research*, **78**(17), 3418–3429.

Japan Meteorological Agency, 2019. Tsunami Warnings/Advisories, Tsunami Information.

Käser, M., Dumbser, M., de la Puente, J., & Igel, H., 2007. An arbitrary high-order Discontinuous Galerkin method for elastic waves on unstructured meshes - III. Viscoelastic attenuation, *Geophysical Journal International*, **168**(1), 224–242.

Lotto, G. C., Dunham, E. M., Jeppson, T. N., & Tobin, H. J., 2017a. The effect of compliant prisms on subduction zone earthquakes and tsunamis, *Earth and Planetary Science Letters*, **458**, 213–222.

Lotto, G. C., Nava, G., & Dunham, E. M., 2017b. Should tsunami simulations include a nonzero initial horizontal velocity?, *Earth, Planets and Space*, **69**(1), 117.

Lotto, G. C., Jeppson, T. N., & Dunham, E. M., 2018. Fully coupled simulations of megathrust earthquakes and tsunamis in the japan trench, nankai trough, and cascadia subduction zone, *Pure and Applied Geophysics*, pp. 1–33.

Meister, O., Rahnema, K., & Bader, M., 2016. Parallel, memory efficient adaptive mesh refinement on structured triangular meshes with billions of grid cells, *ACM Transactions on Mathematical Software*, **43**(3), 19:1–19:27.

Oeser, J., Bunge, H.-P., & Mohr, M., 2006. Cluster design in the earth sciences: Tethys, in *International conference on high performance computing and communications*, pp. 31–40, Springer.

Pelties, C., De La Puente, J., Ampuero, J. P., Brietzke, G. B., & Käser, M., 2012. Three-dimensional dynamic rupture simulation with a high-order discontinuous Galerkin method on unstructured tetrahedral meshes, *Journal of Geophysical Research: Solid Earth*, **117**(2), 1–15.

Pelties, C., Gabriel, A. A., & Ampuero, J. P., 2014. Verification of an ADER-DG method for complex dynamic rupture problems, *Geoscientific Model Development*, **7**(3), 847–866.

Pritchard, M. E., Norabuena, E. O., Ji, C., Boroschek, R., Comte, D., Simons, M., Dixon, T. H., & Rosen, P. A., 2007. Geodetic, teleseismic, and strong motion constraints on slip from recent southern Peru subduction zone earthquakes, *Journal of Geophysical Research*, **112**(B3), B03307.

Rettenberger, S., 2017. PUMGen.

Rettenberger, S., Meister, O., Bader, M., & Gabriel, A.-A., 2016. ASAGI: A Parallel Server for Adaptive Geoinformation, in *Proceedings of the Exascale Applications and Software Conference 2016 on - EASC '16*, pp. 1–9, ACM Press, Stockholm, Sweden.

Ryan, K. J., Geist, E. L., Barall, M., & Oglesby, D. D., 2015. Dynamic models of an earthquake and tsunami offshore Ventura, California, *Geophysical Research Letters*, **42**(16), 6599–6606.

Saito, T., Baba, T., Inazu, D., Takemura, S., & Fukuyama, E., 2019. Synthesizing sea surface height change including seismic waves and tsunami using a dynamic rupture scenario of anticipated Nankai trough earthquakes, *Tectonophysics*, p. 228166.

Seno, T., 2014. Stress drop as a criterion to differentiate subduction zones where M<inf>w</inf>9 earthquakes can occur, *Tectonophysics*.

Sobolev, S. V. & Muldashev, I. A., 2017. Modeling Seismic Cycles of Great Megathrust Earthquakes Across the Scales With Focus at Postseismic Phase, *Geochemistry, Geophysics, Geosystems*, **18**(12), 4387–4408.

Stephenson, W., Reitman, N., & Angster, S., 2017. U.S. Geological Survey Open-File Report 2017–1152: P- and S-wave velocity models incorporating the Cascadia subduction zone for 3D earthquake ground motion simulations, version 1.6—Update for Open-File Report 2007–1348, Tech. rep., U.S. Geological Survey.

Sun, T., Wang, K., Fujiwara, T., Kodaira, S., & He, J., 2017. Large fault slip peaking at trench in the 2011 Tohoku-oki earthquake, *Nature Communications*, **8**, 14044.

Synolakis, C. E., Bernard, E. N., Titov, V. V., Kânoğlu, U., & González, F. I., 2008. Validation and Verification of Tsunami Numerical Models, *Pure and Applied Geophysics*, **165**(11-12), 2197–2228.

Tanioka, Y. & Satake, K., 1996. Tsunami generation by horizontal displacement of ocean bottom, *Geophysical Research Letters*, **23**(8), 861–864.

Ulrich, T., Gabriel, A.-A., Ampuero, J.-P., & Xu, W., 2019a. Dynamic viability of the 2016 Mw 7.8 Kaikōura earthquake cascade on weak crustal faults, *Nature Communications*, **10**(1), 1213.

Ulrich, T., Vater, S., Madden, E. H., Behrens, J., van Dinther, Y., van Zelst, I., Fielding, E. J., Liang, C., & Gabriel, A.-A., 2019b. Coupled, physics-based modeling reveals earthquake displacements are critical to the 2018 Palu, Sulawesi tsunami.

Uphoff, C. & Bader, M., 2016. Generating high performance matrix kernels for earthquake simulations with viscoelastic attenuation, in *2016 International Conference on High Performance Computing & Simulation (HPCS)*, pp. 908–916, IEEE.

Uphoff, C., Rettenberger, S., Bader, M., Madden, E., Ulrich, T., Wollherr, S., & Gabriel, A.-A., 2017. Extreme scale multi-physics simulations of the tsunamigenic 2004 sumatra megathrust earthquake, in *Proceedings of the International Conference for High Performance Computing, Networking, Storage and Analysis, SC 2017*.

USGS, 2019. M 8.4 - near the coast of southern Peru.

van Dinther, Y., Gerya, T. V., Dalguer, L. A., Corbi, F., Funiciello, F., & Mai, P. M., 2013a. The seismic cycle at subduction thrusts: 2. Dynamic implications of geodynamic simulations validated with laboratory models, *Journal of Geophysical Research: Solid Earth*, **118**(4), 1502–1525.

van Dinther, Y., Gerya, T. V., Dalguer, L. A., Mai, P. M., Morra, G., & Giardini, D., 2013b. The seismic cycle at subduction thrusts: Insights from seismo-thermo-mechanical models, *Journal of Geophysical Research: Solid Earth*.

van Dinther, Y., Mai, P. M., Dalguer, L. A., & Gerya, T. V., 2014. Modeling the seismic cycle in subduction zones: the role and spatiotemporal occurrence of off-megathrust events, *Geophysical Research Letters*, **41**(4), 1194–1201.

van Dinther, Y., Preiswerk, L., & Gerya, T., 2019. A Secondary Zone of Uplift Due to Megathrust Earthquakes, *Pure and Applied Geophysics, in press*.

van Zelst, I., Wollherr, S., Gabriel, A.-A., Madden, E., & van Dinther, Y., 2019. Modelling coupled subduction and earthquake dynamics.

Vater, S. & Behrens, J., 2014. Well-balanced inundation modeling for shallow-water flows with Discontinuous Galerkin schemes, in *Finite Volumes for Complex Applications VII – Elliptic, Parabolic and Hyperbolic Problems*, vol. 78 of **Springer Proceedings in Mathematics & Statistics**, pp. 965–973.

Vater, S., Beisiegel, N., & Behrens, J., 2015. A limiter-based well-balanced discontinuous Galerkin method for shallow-water flows with wetting and drying: One-dimensional case, *Advances in Water Resources*, **85**, 1–13.

Vater, S., Beisiegel, N., & Behrens, J., 2019. A limiter-based well-balanced discontinuous Galerkin method for shallow-water flows with wetting and drying: Triangular grids, *International Journal for Numerical Methods in Fluids*, pp. 1–24, online.

Wei, S., Graves, R., Helmberger, D., Avouac, J.-P., & Jiang, J., 2012. Sources of shaking and flooding during the Tohoku-Oki earthquake: A mixture of rupture styles, *Earth and Planetary Science Letters*, **333-334**, 91–100.

Wendt, J., Oglesby, D. D., & Geist, E. L., 2009. Tsunamis and splay fault dynamics, *Geophysical Research Letters*, **36**(15).

Wollherr, S., Gabriel, A.-A., & Uphoff, C., 2018. Off-fault plasticity in three-dimensional dynamic rupture simulations using a modal Discontinuous Galerkin method on unstructured meshes: Implementation, verification, and application, *Geophysical Journal International*, **214**, 1556–1584.

Wollherr, S., Gabriel, A., & Mai, P. M., 2019. Landers 1992 "Reloaded": Integrative Dynamic Earthquake Rupture Modeling, *Journal of Geophysical Research: Solid Earth*, **124**, 2018JB016355.

Table 1. Reference material properties of the SC model. Note that the actual density in the SC model is temperature-dependent, which also affects the seismic velocities. Seismic velocities are calculated assuming a Poisson's ratio of 0.25.

Material	ρ (kg/m^3)	G (GPa)	v_p (m/s)	v_s (m/s)	μ_s^{sc} (-)	μ_d^{sc} (-)	C (MPa)
Sediments	2600	5	2402	1387	0.35	0.105	2.5
Continental crust	2700	12	3651	2108	0.72	0.216	10
Upper oceanic crust	3000	12	3463	2000	0.5	0.15	5
Lower oceanic crust	3000	12	3463	2000	0.85	0.255	15
Mantle	3300	35	5641	3257	0.6	0.18	20

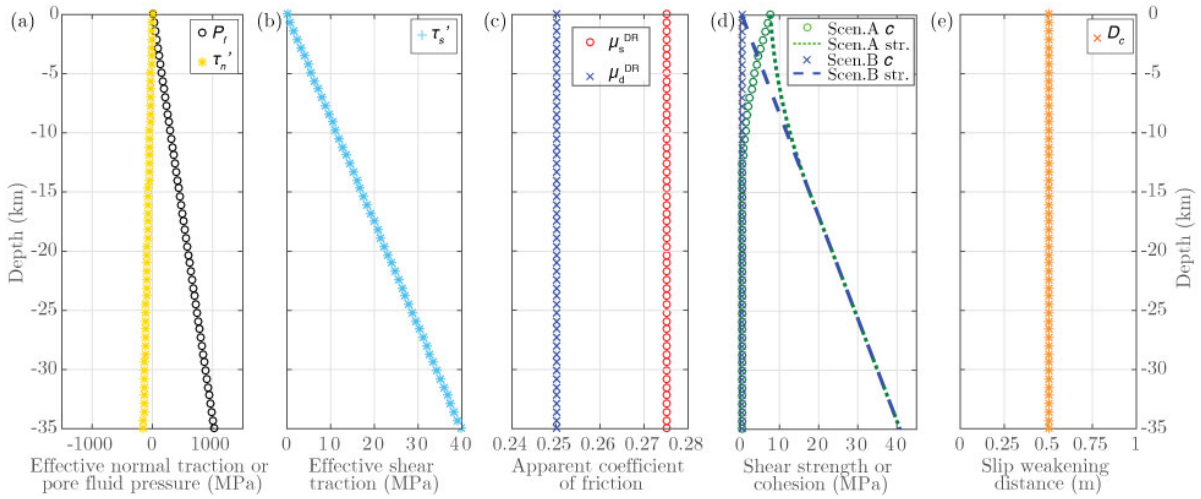

Figure 1. Parameters for the earthquake models in the earthquake-tsunami test case along a cross section at $y = 0$ through the 3D fault: (a) effective normal traction and pore fluid pressure, (b) shear traction, (c) apparent coefficients of static and dynamic friction, (d) on-fault cohesion and fault strength, and (e) slip-weakening distance. Note that only (d) change in the earthquake models for Scenario A and Scenario B.

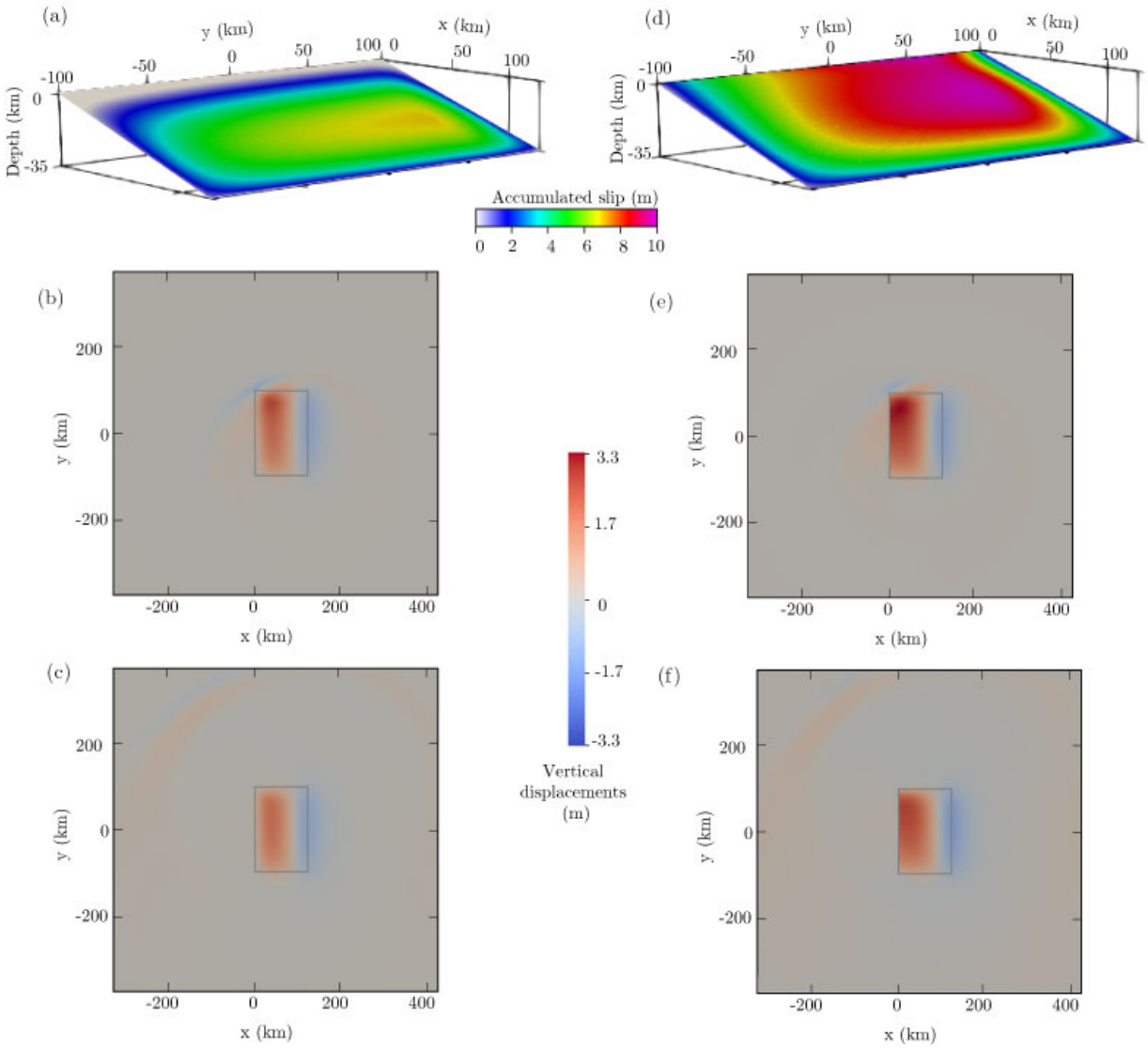

Figure 2. Earthquake scenarios in the earthquake-tsunami test case. For Scenario A: (a) accumulated slip, (b) vertical surface displacements at 56 s (time of maximum uplift) and (c) final vertical displacements. For Scenario B: (d) accumulated slip, (e) vertical surface displacements at 56 s (time of maximum uplift) and (f) final vertical displacements.

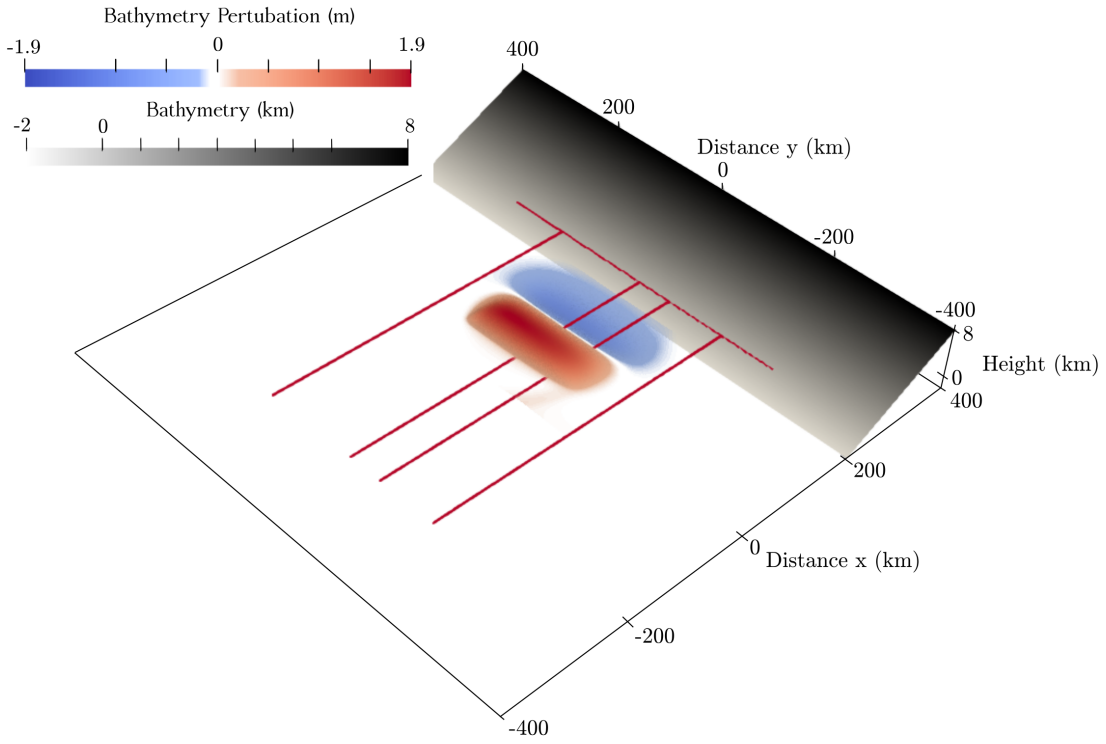

Figure 3. Bathymetry (flat seafloor) and bathymetry pertubation ($\Delta b(t, x, y)$) from the Scenario A earthquake at $t = 102$ s for the tsunami model in the earthquake-tsunami test case. In red are lines at $y = -150.0$ km, $y = -54.8$ km, $y = 0$, and $y = 150.0$ km and points along the beach at $x = 240.0$ km.

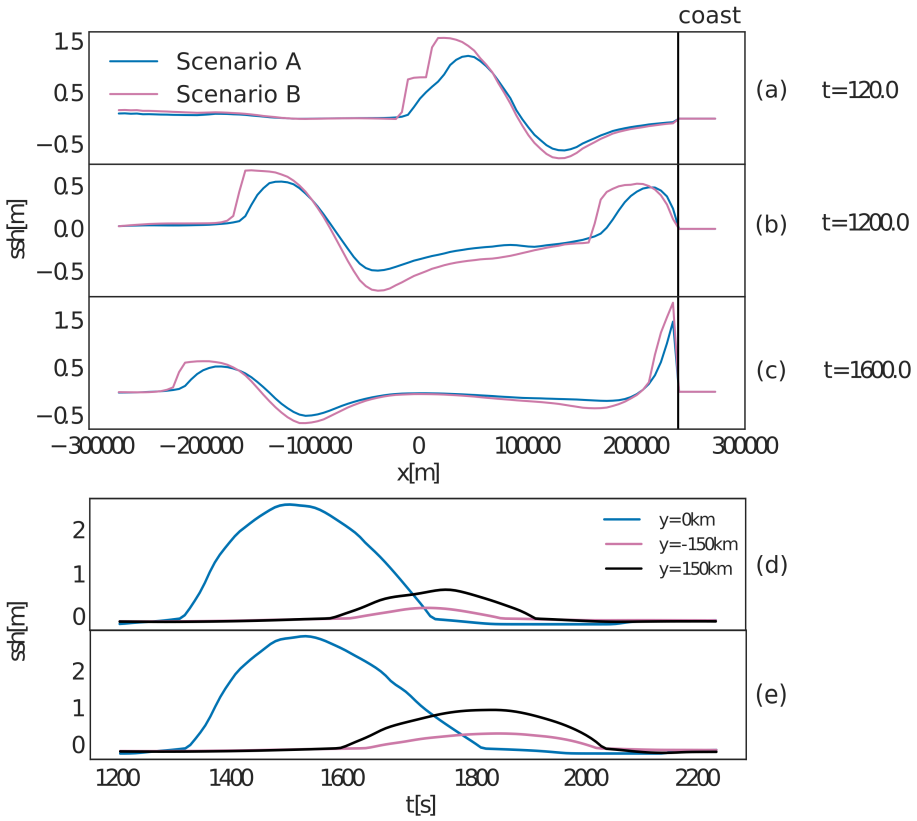

Figure 4. Sea surface height (ssh) in the tsunami scenarios from the earthquake-tsunami test case along a cross section at $y = -54.8$ km and at (a) the end of the earthquake, (b) the approximate time of the first inundation, and (c) the approximate time of maximum inundation. Time series of ssh at 3 probes located 10 m from the coast at $x = 240.1$ km for (d) Scenario A and (e) Scenario B.

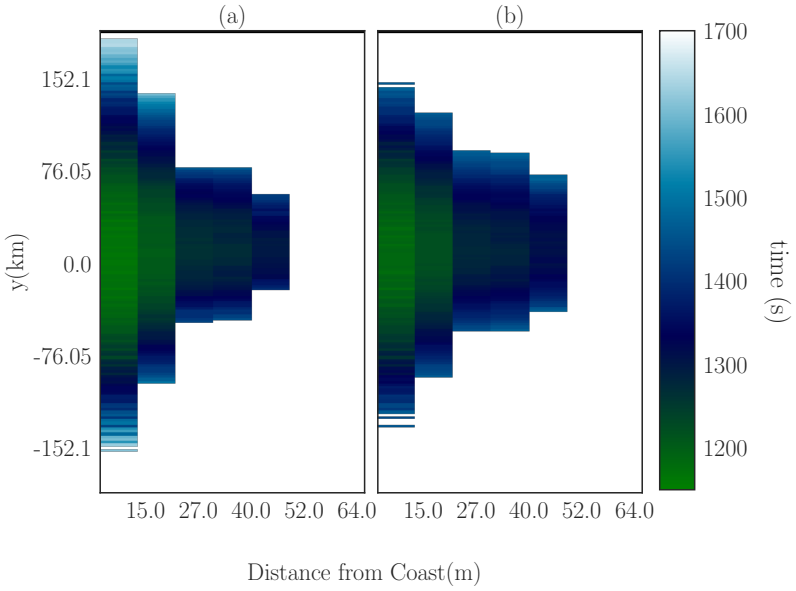

Figure 5. Color plot of inundation over time for the tsunami scenarios from the earthquake-tsunami test case: (a) Scenario A and (b) Scenario B. The coast is located at $x = 240$ km. Time is the model time at which the location is first inundated. The stepwise inundation distribution is due to the mesh resolution near the coast.

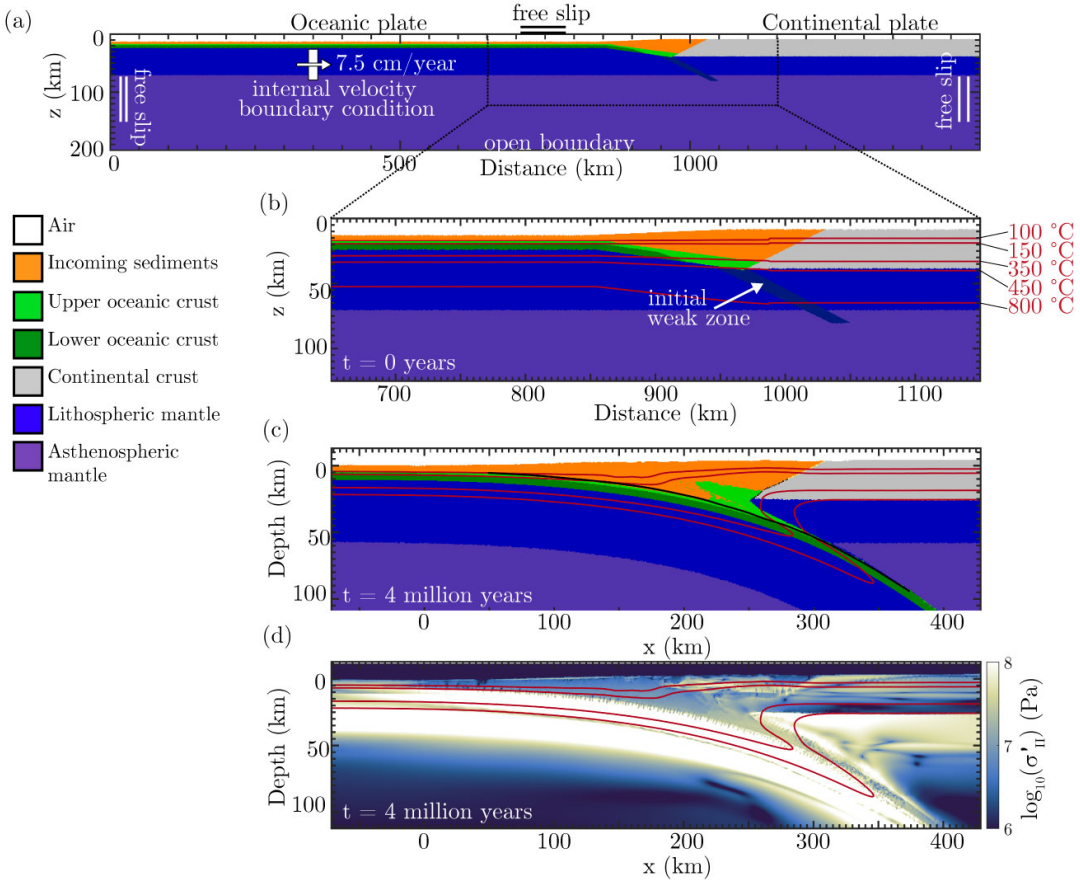

Figure 6. (a,b) Set-up of the subduction physical model and (c) final geometry of the subduction zone at the approximate time of the subduction slip event used in the subduction-earthquake-tsunami test case. (d) Log of the second invariant of the deviatoric stress tensor, σ'_{II}, which controls yielding in the subduction model (see Eq. 3). Note that the coodinates change from (a,b) to (c,d).

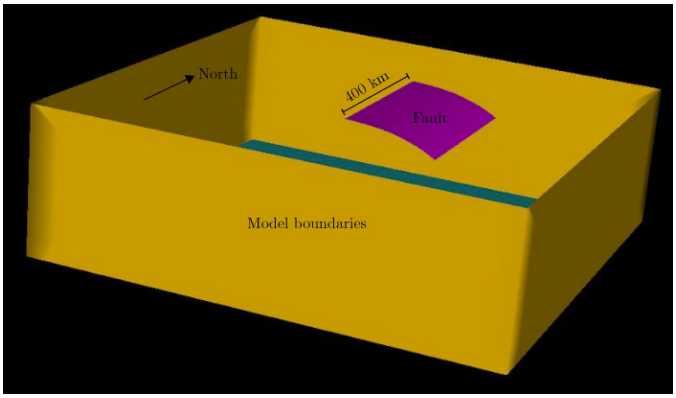

Figure 7. Structure of the earthquake model in the subduction-earthquake-tsunami test case. Volume (yellow) is 1600 km along each side and 500 km deep. Fault (pink) is 400 km along strike.

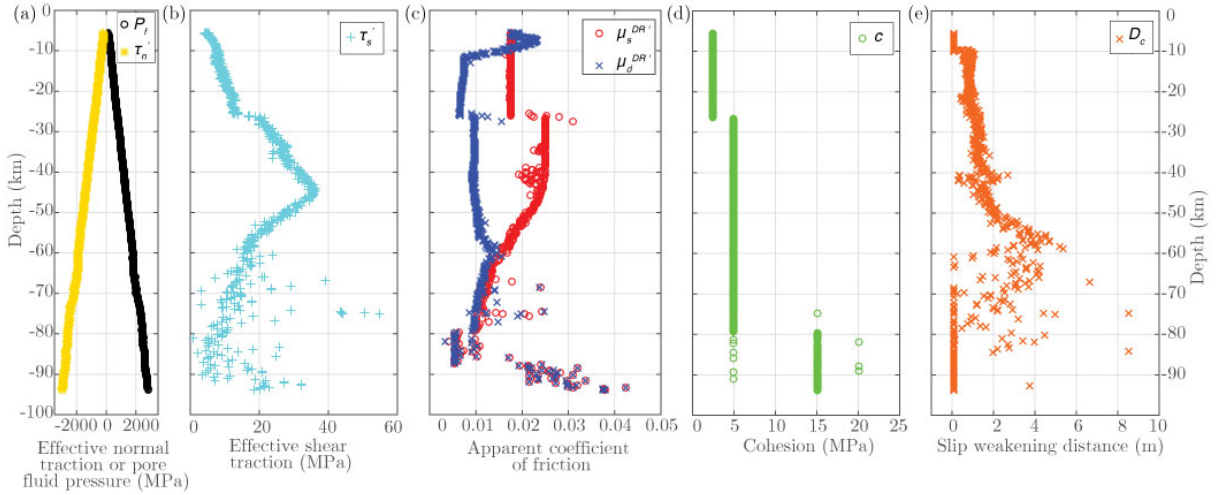

Figure 8. For the earthquake model in the subduction-earthquake-tsunami test case: variation along a cross section at $y = 0$ through the 3D fault of (a) normal traction and pore fluid pressure, (b) shear traction, (c) static and dynamic friction coefficients, (d) on-fault cohesion and (e) slip-weakening distance. Values are before corrections are made to c in the sediments and to $\mu_s^{\rm dr}$ at outliers, as discussed in text.

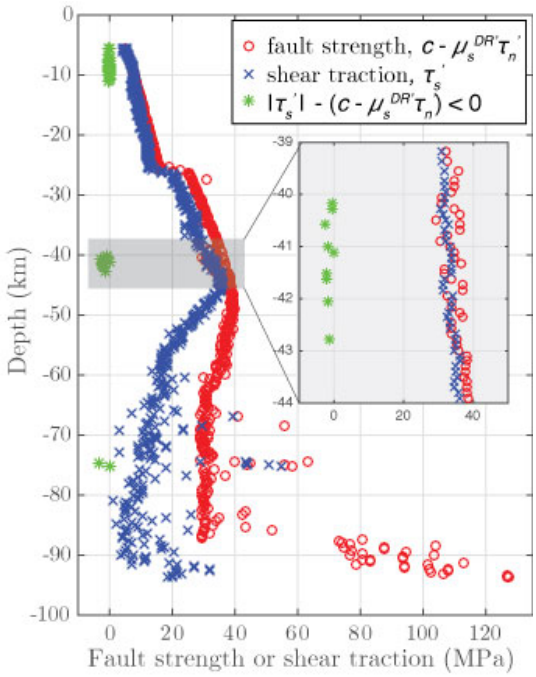

Figure 9. (a) Failure analysis according to the earthquake model failure criterion at points along a cross section at $y = 0$ through the 3D earthquake model fault. Variables are defined in the text near Eq. 1. Green stars are locations initially at failure, before changes are made to c in the sediments and to $\mu_s^{\rm dr}$ at several outliers, as discussed in the text. Zoom is to region near the nucleation zone.

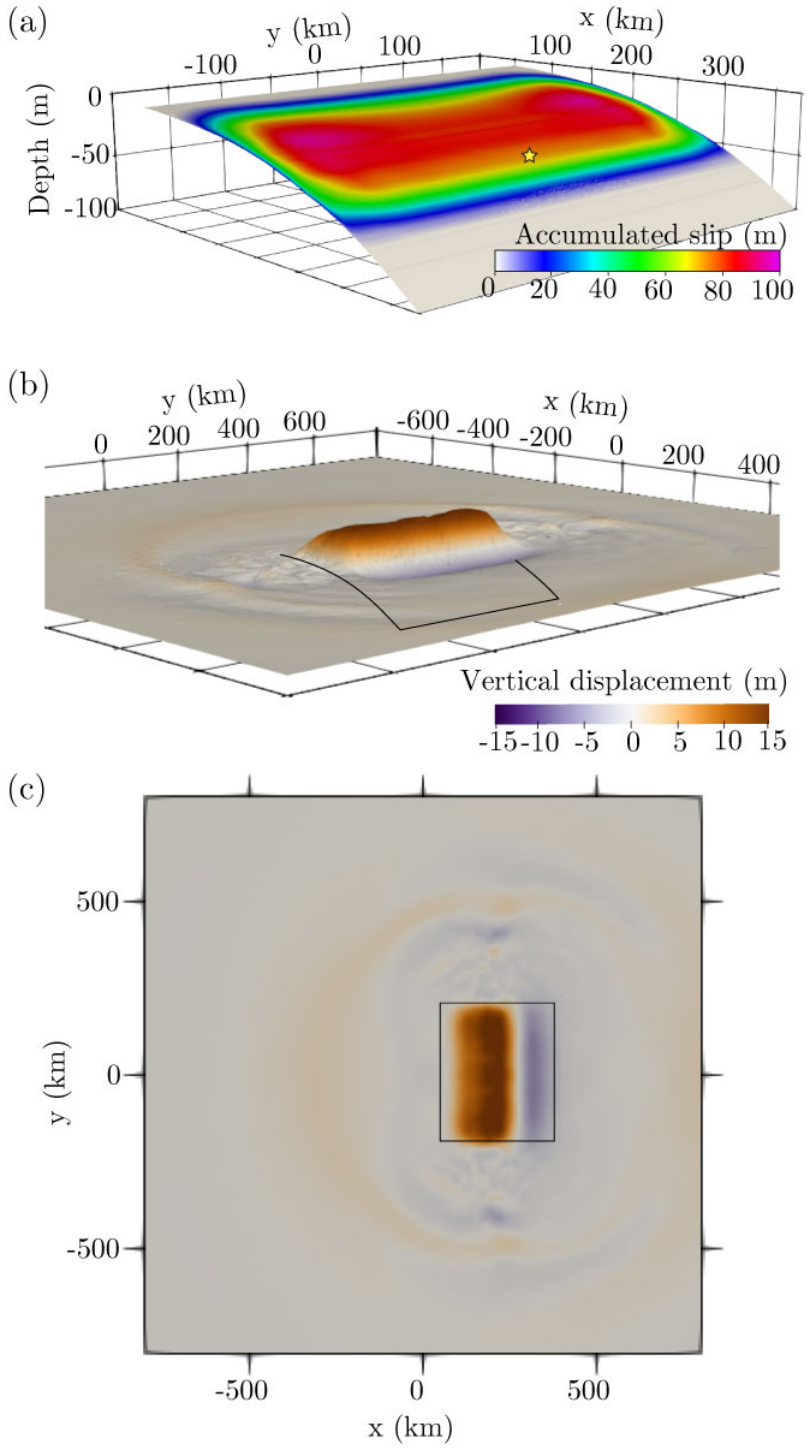

Figure 10. Earthquake scenario from the subduction-earthquake-tsunami test case at $t = 230\ s$: (a) accumulated slip on the fault, (b) oblique view of the vertical surface displacements, and (c) map view of the vertical surface displacements. Black lines in (b) and (c) outline the fault.

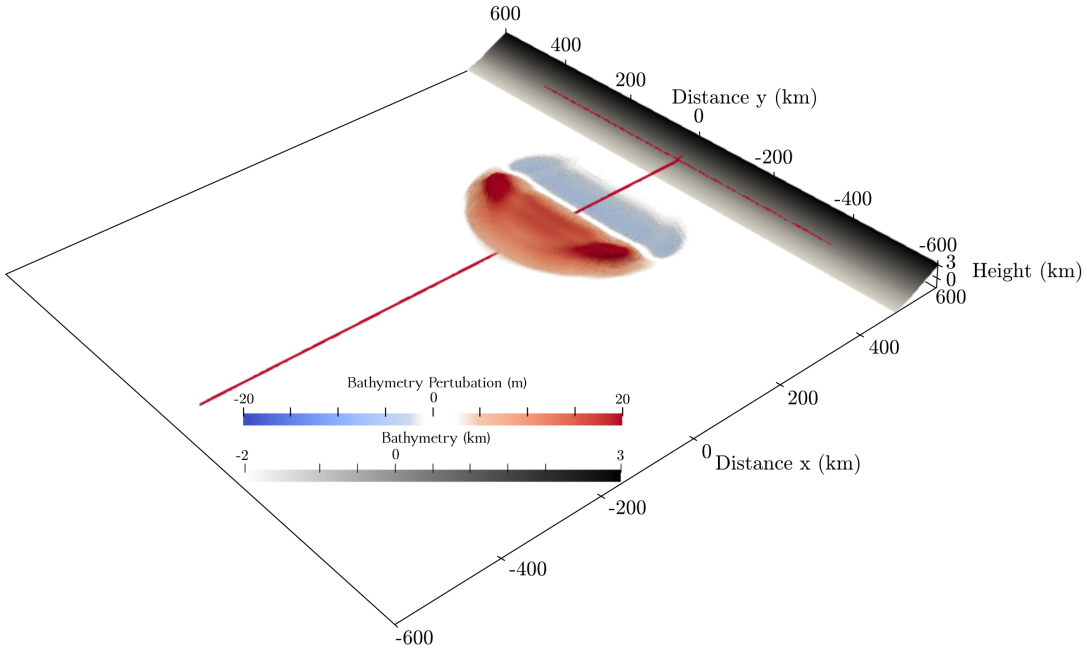

Figure 11. Bathymetry with bathymetry pertubation ($\Delta b(t, x, y)$) at $t = 100$ s for the tsunami model in the subduction-earthquake-tsunami test case. A line at $y = 0$ and the coast at $x = 540$ km are marked in red.

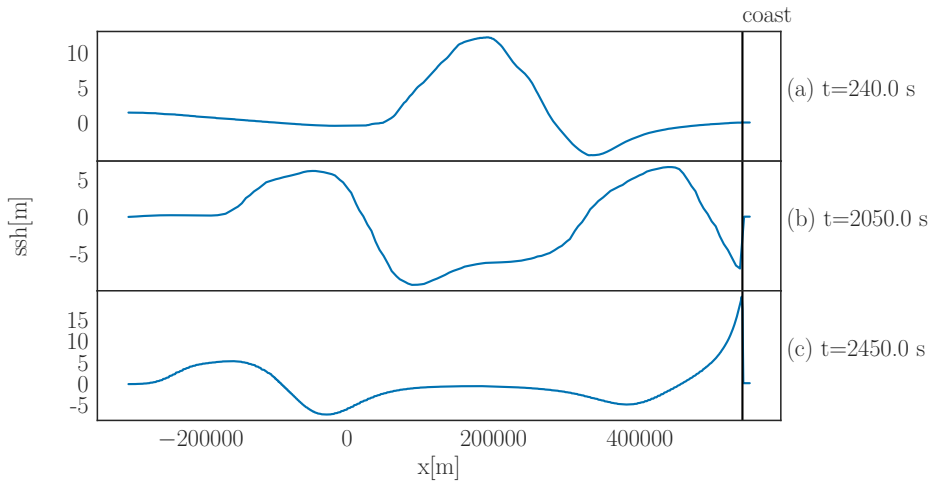

Figure 12. Sea surface heights (ssh) from the tsunami scenario in the subduction-earthquake-tsunami test case along $y = 0$ at (a) the end of the earthquake, (b) the approximate time of first inundation and (c) the approximate time of maximum inundation.

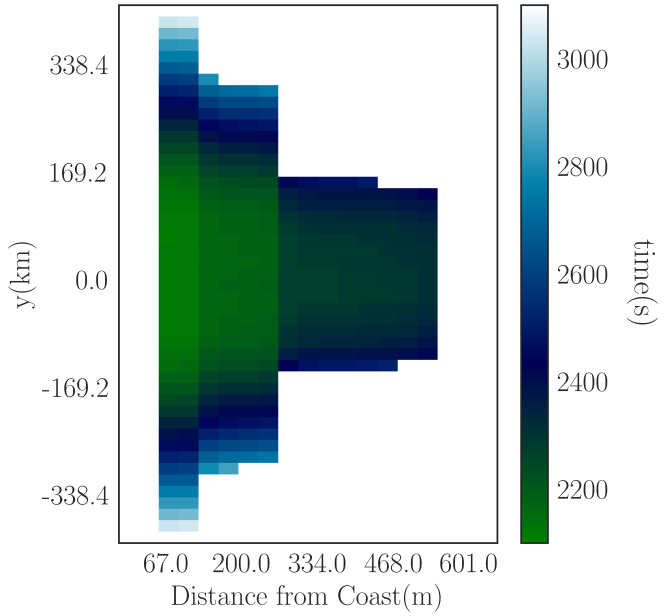

Figure 13. Inundation in space and time for the tsunami scenario in the subduction-earthquake-tsunami test case. The coast is located at $x = 540$ km.

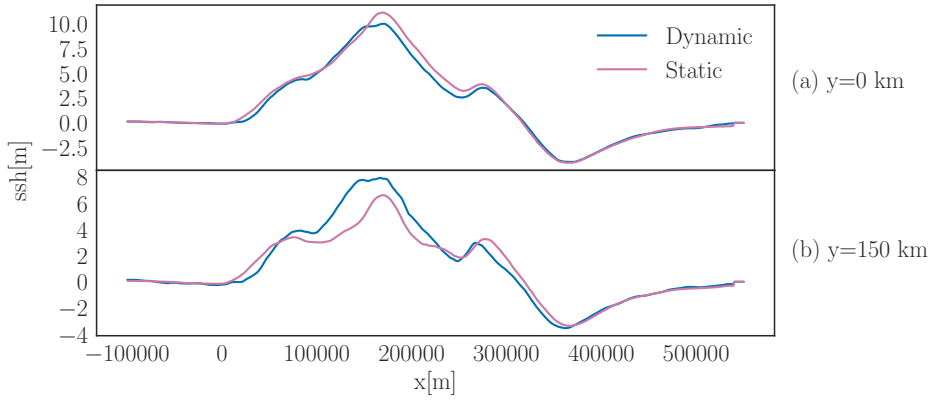

Figure 14. Comparison of sea surface heights (ssh) from statically and dynamically sourced tsunamis at $t = 420$ s for cross sections at (a) $y = 0$ km and (b) $y = 150$ km.

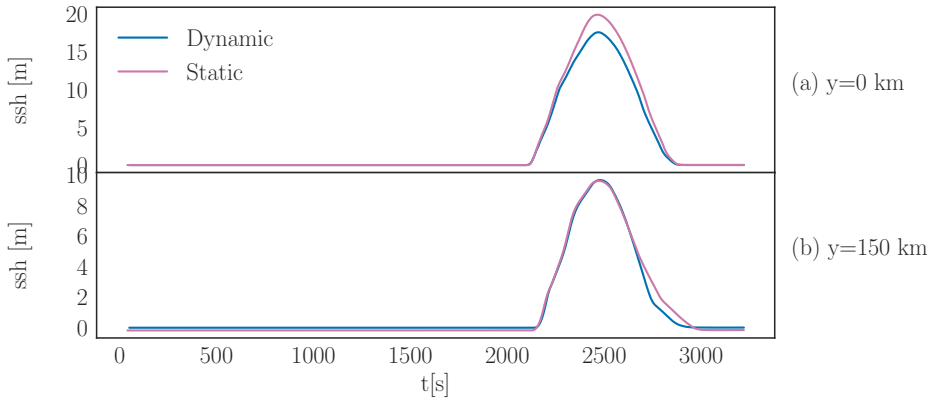

Figure 15. Comparison of sea surface heights (ssh) over time for the statically and dynamically sourced tsunamis at points on the coast at (a) $x = 540$ km and $y = 0$ km, and (b) $x = 540$ km and $y = 150$ km.

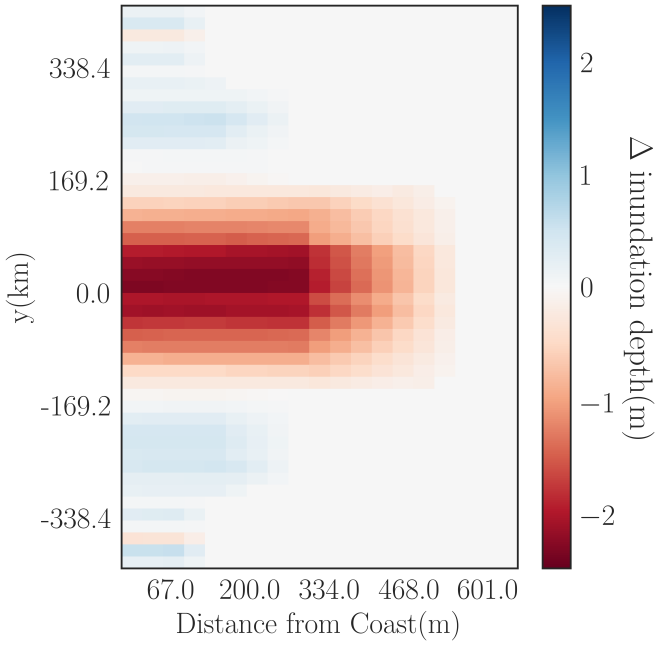

Figure 16. Difference in maximum inundation depth between dynamically and statically sourced tsunamis (dynamic minus static).

APPENDIX A: MATERIALS FOR RUNNING THESE TEST CASES

The materials required to run the earthquake and tsunami models involved in these test cases are provided on Google Drive at `https://bit.ly/2NmM57q` and later will be shared on `www.zenodo.org`. Outputs for the STM, earthquake and tsunami models also are provided. Details about these files and additional technical information for running both test cases are outlined in the following sections.

APPENDIX B: WHERE TO FIND THE COMPUTATIONAL MODELS

The STM code used to model long term subduction links geodynamics and seismic cycling. It is not publicly available.

SeisSol is used for the dynamic earthquake rupture models presented here. It is available at `https://github.com/SeisSol/SeisSol` along with compilation instructions, a user manual and examples. Information also is available at `http://www.seissol.org`.

sam(oa)^2 is used for the tsunami models presented here. It is available at `https://gitlab.lrz.de/samoa/samoa`.

APPENDIX C: MODELING DETAILS FOR THE EARTHQUAKE-TSUNAMI TEST CASES

C1 The earthquake model with SeisSol

The earthquake physical model includes an elastic constitutive law, a dynamic earthquake source, and a linear slip-weakening friction law. Running the model requires several input files: the mesh, a parameter file (.par) providing modeling choices, such as the selected friction law and sampling rates, one easi file (.yaml) that sets the stress and assigns the frictional parameters, and one easi file (.yaml) that sets the material properties. easi is the Easy Initialization Library (`www.github.com/SeisSol/easi`) and the two .yaml files configure the SeisSol input.

The structural model and mesh both are generated with the open-source software Gmsh (`www.gmsh.info`) (Geuzaine & Remacle 2009). Mesh structure and resolution are set in a .geo file. This is optimized and converted to a .msh file as:

```
>> gmsh xxx.geo -3 -optimize
```

Then, the .msh is converted to the gambit mesh format (.neu) using `gmsh2gambit`, which is provided with SeisSol. It is now possible to combine these 2 steps into one as:

```
>> gmsh xxx.geo -3 -optimize -format neu
```

Meshing is performed with the software PUMGen (`https://github.com/SeisSol/PUMGen/`) (Rettenberger 2017), which also exports the mesh into the efficient PUML format used by SeisSol. PUMGen embeds MeshSim from SimMetrix, the underlying mesh generator of SimModeler (`www.simmetrix.com`), such that the mesh generation may be run in parallel on a compute cluster. This is crucial for generating high-resolution meshes of hundreds of millions of elements (e.g. Uphoff et al. (2017)). This mesh was created on 1 node in a few minutes.

The resolution of the mesh is 400 m on the fault. The model order of accuracy, set to 6, sets the number of additional on-fault integration points and results in an actual on-fault resolution of $400/6 = 66$ m. The mesh coarsens gradually off the fault to a maximum mesh size of 100 km. The resulting mesh consists of 16 million tetrahedral elements. Following (Wollherr et al. 2018), and using the script `Calc_CohesiveZoneError.py` available with SeisSol, we determine the following expected average errors for the model results for this mesh: 0.09% for the rupture arrival, 7.6% for the peak slip rate, and 0.8% for the final slip magnitude. These meet the recommendations from Day et al. (2005) for acceptable errors, as follows: rupture arrival below 0.2%, peak slip rate below 7% and final slip below 1%. However, we note that these are derived for a different model set-up.

Nucleation occurs in a predefined region on the fault with a reduced mesh element edge length of 250 m. Failure initiates and becomes a sustained rupture as the friction is decreased over time in this patch, as specified in the easi file (.yaml) for setting the stress and frictional properties, in lines 17–24.

We provide the .geo, .msh, .neu and final mesh files. The final mesh files are an .xdmf file and a file with the same name, but no explicit format.

We provide the output for both scenarios along the fault and at the surface. We view the model results in Paraview (`https://www.paraview.org`). Each set of output consists of 3 files that must be in the same folder, then the .xdmf file is opened in Paraview. We used the predefined filter to convert cell data to point data before calculating maxima, minima and averages.

C2 The tsunami model with sam(oa)^2

Running the tsunami models requires two input files which hold the converted displacement fields on uniform meshes. The corresponding bathymetry is set in the compilation configuration, which is build on Scons.

As temporal and spatial scales differ between the earthquake and tsunami models linked here, several adjustments of the seafloor displacement fields were made. The raw displacements are provided as the earthquake model output. We provide with the tsunami materials the filtered bathymetry perturbations for both scenarios, a list of measured coordinates, and the required compilation configuration to run the models. We also provide the output of the tsunami scenarios at the given positions and supplementary videos of the wave fields.

For the temporal filtering, we provide a python script to reproduce our approach. To apply temporal filtering, we first generate the time-frequency representation of the earthquake displacement field at positions where Rayleigh waves appear exclusively. For the two earthquake scenarios in the earthquake-tsunami test case, the measured frequencies lie in a range of [0.004,0.015] Hz. For reference, we do same analysis close to the center of the displacement fields and the measured frequency range is [0.0001,0.01] Hz. The premise of this temporal filtering approach is to filter out measured

frequency ranges of Rayleigh waves as well as possible, while leaving the reference close to the earthquake as untouched as possible. In these earthquake scenarios, the ranges are close to each other, or even overlap, so the filter requires a steep descent between the high frequency stop band and the low frequency pass band. Butterworth filters of high order, in this case order 10 and 11, show this high descent and are numerically stable. We use order 11 for the tsunami models in this test case. We do an a posteriori analysis of the frequency ranges of the temporally filtered displacement fields, to see how well the Rayleigh waves are filtered out and how much the filter affects the displacement field close to the center of the earthquake. Repeating this routine and adjusting the threshold leads to the chosen cut-off frequencies.

SeisSol produces surface displacements on an unstructured triangular mesh, in which each cell holds the averaged displacement. sam(oa)^2 utilizes an adaptive refined triangular mesh. Therefore, we project the displacements from the earthquake scenario onto a uniform intermediate grid of constant resolution. Tests show that a resolution of 1000 m is sufficient to represent the displacement field and higher resolutions only lead to marginal improvements. The result is linearly interpolated and assigned as an initial condition in the tsunami model by the ASAGI library (see Sec. 2.4). The projected displacements are generated with a custom script that can be found at `https://gitlab.lrz.de/samoa/displacement-converter.git`.

We run the tsunami model with a mesh resolution of 3125 m to 12.2 m. Dry tolerance is set to 0.01 m. Adaptive Mesh Refinement is set to keep the highest resolution along the coast, while cells inside the ocean are refined based on an error estimate. We generate the maximum and minimum gradient of the sea surface height (ssh) (water column + bathymetry) for all cells. Cells that are within a 1% range of the minimum are coarsened, while cells within 10% of the maximum error are refined.

APPENDIX D: MODELING DETAILS FOR THE SUBDUCTION-EARTHQUAKE-TSUNAMI TEST CASE

D1 The seismo-thermo-mechanical subduction model

The seismo-thermo-mechanical (STM) model has minimum resolution of 500 m in the subduction channel and a maximum resolution of 2000 m at the model edges. The final grid consists of 1654×270 nodes. A maximum of 51.6 million markers is used to track the materials.

We provide the section of the model output that is used as input for the earthquake model in a text file. This information is on a grid comprised of 1800 points in the x-direction and 1034 points in the z-direction at a resolution of 500 m. It covers a region that extends from $x = -174.75$ to 724.75 km and from $z = 11.75$ to -504.75 km. This region is shorter in the x-direction and longer in the z-direction than the subduction model domain. Values in the text file that are beyond the subduction model limits are copied from the closest depth and repeat. The region in the text file is also slightly larger than the region originally cut from the subduction model output, so values also repeat near the x-limits of the text file as well. This reflects the methods for linking a subduction slip event to a 2D SeisSol earthquake model, for which the text file must cover the entire earthquake model domain (van Zelst et al. 2019). Note that values at the limits of the provided text file do not affect behavior in this model. We provide these details only so that the interested modeler knows exactly what is provided. However, other physical models might require different procedures for porting the subduction model output to the earthquake model.

The 2D fault coordinates, determined after the slip event is complete, also are provided as a text file.

D2 The earthquake model with SeisSol

D2.1 SeisSol earthquake model

The earthquake physical model uses the fault geometry and initial conditions from the selected subduction slip event. The physical model domain extends from $x = -800$ to 800 km, $y = -800$ to 800 km and $z = -500$ to 0 km. The fault dips, with limits at $y = -200$ and 200 km, $x = 50$ and 373 km and $z = -6$ and -95 km. It does not intersect the surface. We use GOCAD (`www.pdgm.com`) to build the structural model for the SeisSol earthquake model. We build the fault by following these steps:

(i) Import fault x, z data as Cultural Data from the provided text file
(ii) Select "closed curve"
(iii) Filter every 5000 m
(iv) Copy curve to desired y-locations
(v) Create 1 curve from all curves
(vi) Bridge nodes from every other set of neighboring curves at top of fault, then connect opposite neighbors at bottom of fault, making a zig-zag
(vii) Create new points set from this curve
(viii) Create new surface from this points set
(ix) Export from GOCAD as Surface > DXF file

NB: Do not beautify triangles on fault, as this distorts fault shape. We provide the GOCAD project files.

We use SimModeler (`www.simmetrix.com`) with PUMgen to generate the mesh (Fig. A1). First, the GOCAD file must be converted to an .stl file format. Execute `convertDXFtoStl.py` (available with SeisSol) as:

```
>> python convertDxf2Stl.py --isolate xxx.dxf
```

To show all options, use `-h`.

Launch SimModeler and import the .stl file as "discrete data". Using "isolate" in the .dxf to .stl conversion means that, when opened in SimModeler, you do not need to specify angles that separate regions from one another and can leave the boxes unchecked. Next, set the Meshing and Analysis parameters. We used the following values:

(i) gradation rate = 0.3
(ii) aspect ratio = 8.0
(iii) volume ratio = 12.0
(iv) on-fault mesh resolution = 400 m
(v) volume mesh resolution = 100000 m

We provide the .dxf, .stl and .smd (SimModeler) files.

We generate the mesh with PUMGen, as done for the earthquake model in the earthquake-tsunami test case (Fig. A1a). The mesh size is 43 mio elements with a minimum in-sphere of 18 m. The model order of accuracy of 6 sets the number of additional on-fault integration points, resulting in an actual on-fault resolution of $400/6 = 66$ m. As for the model in the earthquake-tsunami test case, we accurately resolve the estimated minimum cohesive zone width of 150 m (Wollherr et al. 2018) and the same errors are expected.

We also tested and provide a 13 mio element mesh that balances element sizes more efficiently. This mesh has an element edge length resolution of 1 km on the fault, 5 km within a mesh refinement zone surrounding the fault, and a maximum element edge length of 20 km. We used the following values:

(i) gradation rate $= 0.3$
(ii) aspect ratio $= 6.0$
(iii) volume ratio $= 12.0$
(iv) on-fault mesh resolution $= 1000$ m
(v) volume mesh resolution $= 20000$ m
(vi) mesh refinement cube $= 5000$ m

For this mesh, instead of resolving the minimum cohesive zone width on the fault (150 m), we take the 15th percentile (225 m), determined using the script `estimateMinimumCohesiveZone.py` that is provided with SeisSol. We find no difference in the results from the model run with this versus the original mesh. We also note that this model was run for 420 s and the slow waves in the sediments near the surface persist at this point in time (see Sec. 4.2.2 and Fig. 10b, c).

D2.2 Running the SeisSol earthquake model

The earthquake physical model includes an elastic constitutive law, a dynamic earthquake source, and a linear slip-weakening friction law. Running the model requires several input files: the mesh, three NetCDF files (.nc) containing the input parameters, a parameter file (.par) calling on those files and providing additional modeling choices, and two easi files (.yaml) that configure the SeisSol input. We provide each of these files, as well as the model output.

Three 2D NetCDF files are created from the provided text file of subduction model output using the provided Matlab script. These NetCDF files use the exact points provided in the text file at 500 m resolution (i.e. no interpolation). The three NetCDF files separately contain (1) the material properties shown in Fig. A2, (2) the stress field and on-fault frictional parameters reflecting the values shown in Fig. 8 except for the static friction coefficient, and (3) the static friction coefficient. For SeisSol, it is helpful to keep the static friction coefficient separate in this way because it is used in the nucleation process. The material properties and on-fault information are kept separate from one another so that they can cover different spatial domains, if desired.

These NetCDF files are converted to the format used by SeisSol by running the `asagi2paraview` tool once. Both the original and the converted (including `conv` in the name) are provided. This tool is available with ASAGI (see Sec. 2.4 and `www.github.com/TUM-I5/ASAGI`). Running the tool again converts the NetCDF file back to the original format.

The 2D information from these NetCDF files is mapped into the third dimension (in the y-direction) during the SeisSol model run by the Easy Initialization Library, easi (`www.github.com/SeisSol/easi`). This is done according to the two .yaml files, one setting the material properties and one setting the stress field and frictional parameters. In addition, any part of the earthquake model domain outside of the region covered by the NetCDF in the x- and z-directions is assigned information from the closest point. This capability allows the 2D NetCDF files to reflect the region of the provided subduction model output (here $x = -174.75$ to 724.75 km, $z = -504.75$ to 11.75 km), but provide input for the entire earthquake model domain (here $x = -800$ to 800 km, $y = -800$ to 800 km and $z = -500$ to 0 km).

Note that, in this earthquake model, a linear elastic constitutive law is used. The material properties are required everywhere throughout the earthquake model domain, while information about the stress field and frictional properties are required only on the fault. Different constitutive relations require different input configurations. For example, if a viscoplastic rheology is invoked (e.g., Wollherr et al. 2018), a stress tensor must be assigned to all locations in the model domain.

We provide the model output along the fault and at the surface. Each consists of 3 files. We view the model results in Paraview (`https://www.paraview.org`) by loading the .xdmf file, but all 3 output files must be in the same folder. Using a predefined filter in Paraview, we converted cell data to point data before calculating maxima, minima and averages.

D2.3 Assessment of accuracy in mapping the slip event conditions to the earthquake model

For accurate mapping of subduction model parameters to the earthquake model, it is critical that the faults in both models are the same shape. This ensures that they experience the same stress field and host the same on-fault properties. To test this, before running the earthquake model, we compare fault locations, fault dip, effective shear traction, and failure on the 2D subduction model fault and along a 2D slice at $y = 0$ through the 43 mio earthquake model mesh. The subduction model fault has 649 locations and the slice through the earthquake model fault has 849 fault locations. As detailed below, we find that the the two faults have the same shape and capture the same initial conditions.

Fig. A3a shows that the differences between fault locations are below the 500 m by 500 m resolution of the subduction model output that is supplied to the earthquake model. Fig. A3b shows that the profile of the earthquake model fault is slightly smoother, without the very small variations in dip along the subduction model fault. Along the subduction model fault, the average dip is 14.8°, the minimum dip is 2.3°, and the maximum dip is 34.4°. Along the slice through the earthquake model fault, the average dip is 14.9°, the minimum dip is 2.8°, and the maximum dip is 31.8°.

Variation in shear traction along both faults with depth is shown in Fig. A4. The two model fault host shear tractions that are free of any systematic differences. Along the subduction model fault, the average shear traction magnitude is 14.9 MPa, the minimum is 1.3 MPa, and the maximum is 54.5 MPa. Along the slice through the earthquake model fault, the average shear traction magnitude is 15.0 MPa, the minimum is 0.9 MPa, and the maximum is 54.7 MPa.

Fig. A4 shows at each depth the shear traction, the static fault strength, and any points at failure, where the absolute magnitude of the shear traction exceeds the fault strength. Both faults have the same regions at failure: within the sediments and near 42 km depth, where the subduction slip event begins and where we set the nucleation zone in the earthquake model. A focus on this region reveals that it extends for $\sim$ 3 km with depth along both faults. Note that the slice through the earthquake model fault has more points at failure here, because it has more fault locations overall.

D3 The tsunami model with sam(oa)^2

Running the tsunami model requires a single file holding the converted displacement field. Bathymetry is again set in the compilation configuration. We provide filtered bathymetry perturbations, a

list of coordinates to generate the presented results and the required compilation configuration to run the model. We also provide the output of the simulation at the given coordinates and a supplementary video.

As for the earthquake-tsunami test case, we temporally filter and project the bathymetry perturbations. See also the explanations in App. C2. For the spectral analysis for temporal filtering, we choose to analyze the point $(x, y) = (-200$ km, 0 km) to track Rayleigh waves. To apply temporal filtering, we first generate the time-frequency representation of the displacement field at positions where Rayleigh waves appear exclusively. For this test case, the measured frequencies lie in a range of [0.016,0.025] Hz. We do the same analysis close to the center of the earthquake and the measured frequency range is [0.001 - 0.01] Hz. We apply an order 10 Butterworth (low-pass) filter.

SeisSol produces the surface displacement field on an unstructured triangular mesh, while sam(oa)^2 utilizes an adaptive refined triangular mesh. Therefore, we project the displacements onto a uniform intermediate grid with a resolution of 1000 m, as for the tsunami model in the earthquake-tsunami test case. The result is linearly interpolated and assigned as an initial condition by the ASAGI library (see Sec. 2.4). The projected displacements are generated with a custom script that can be found at `https://gitlab.lrz.de/samoa/displacement-converter.git`.

The model mesh has a resolution of 4687 m to 36 m. Dry tolerance is set to 0.01 m. See Sec. C2 for information about Adaptive Mesh Refinement.

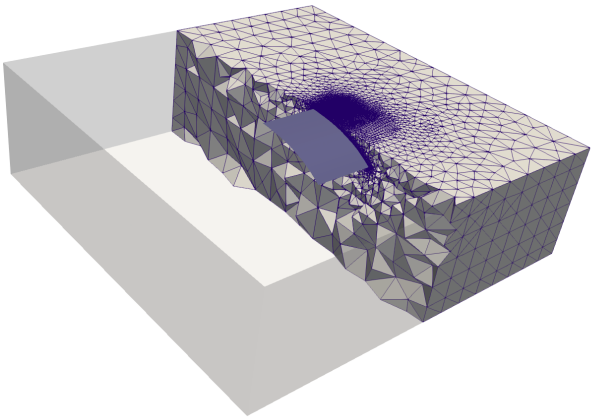

Figure A1. 43 mio element mesh used for the SeisSol earthquake model in the subduction-earthquake-tsunami test case.

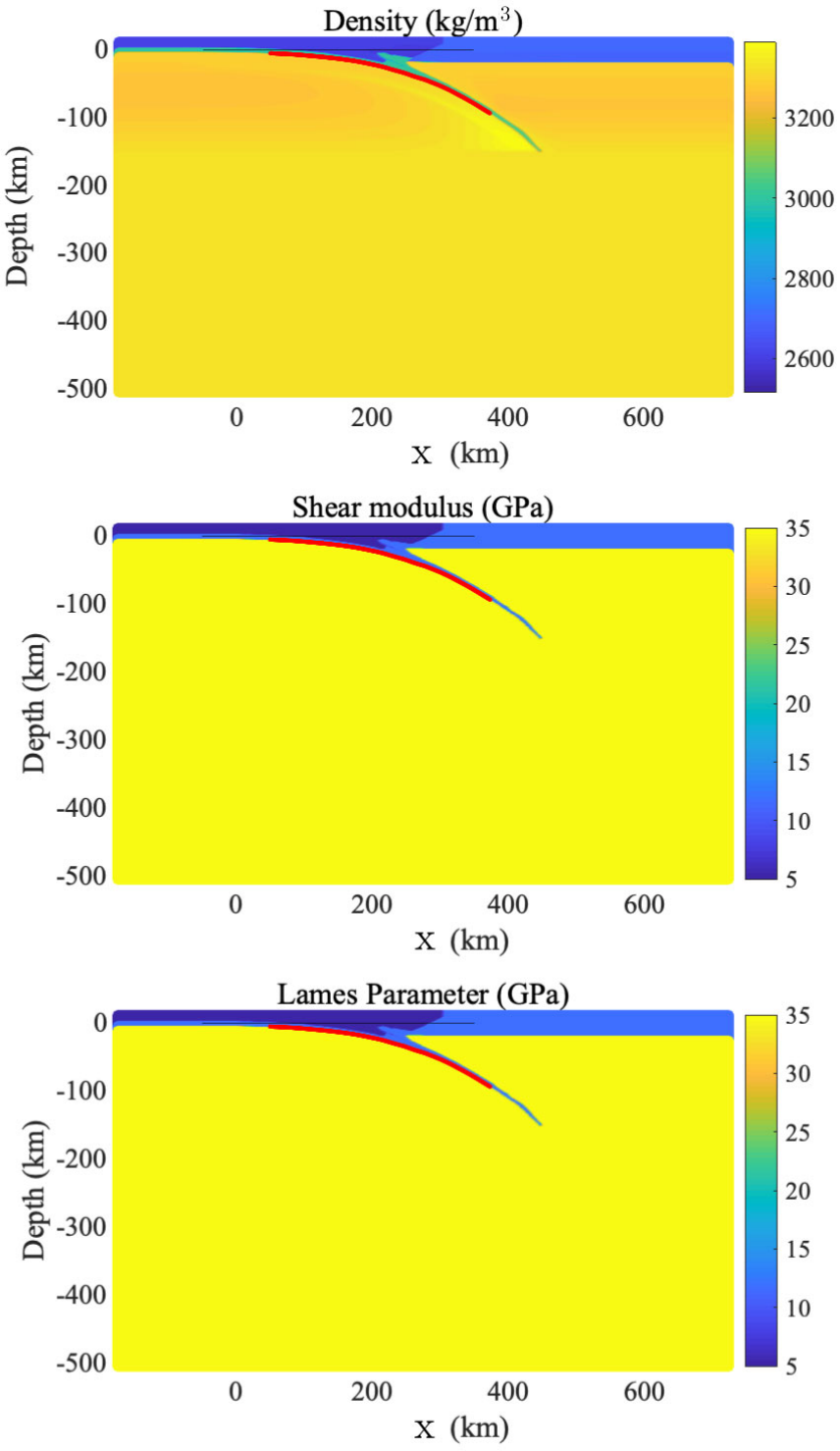

Figure A2. Material properties from the subduction slip event linked to the earthquake model in the subduction-earthquake-tsunami test case. Red curve is the fault that develops in the subduction slip event. Lame's parameter is equal to the shear modulus here, because a Poisson's ratio of 0.25 is used (see text).

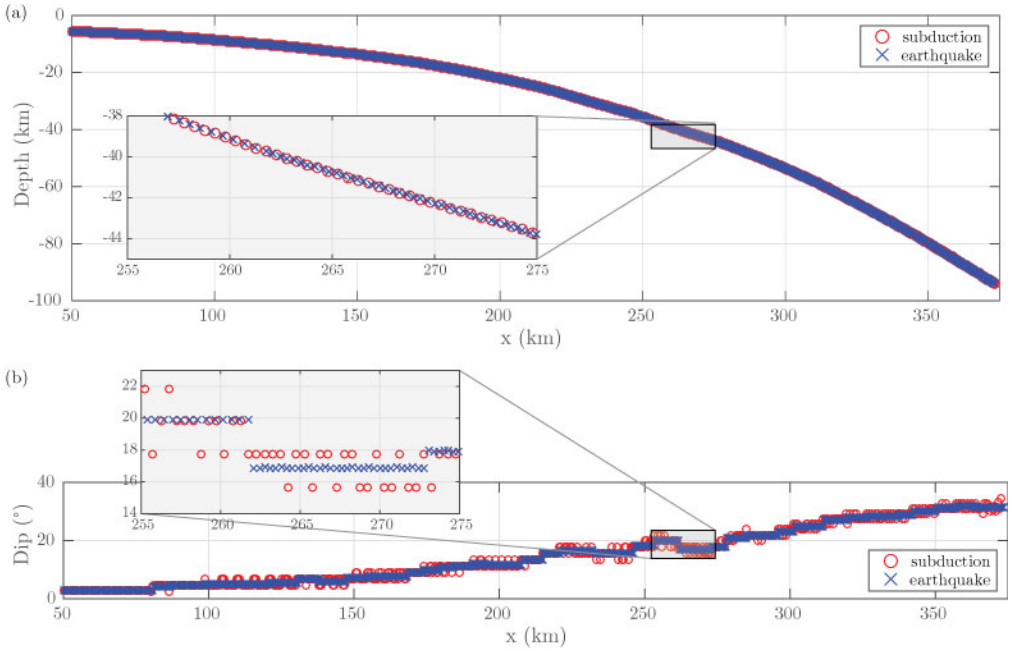

Figure A3. Comparison between (a) locations and (b) dip of faults in the earthquake and subduction models for the subduction-earthquake-tsunami test case.

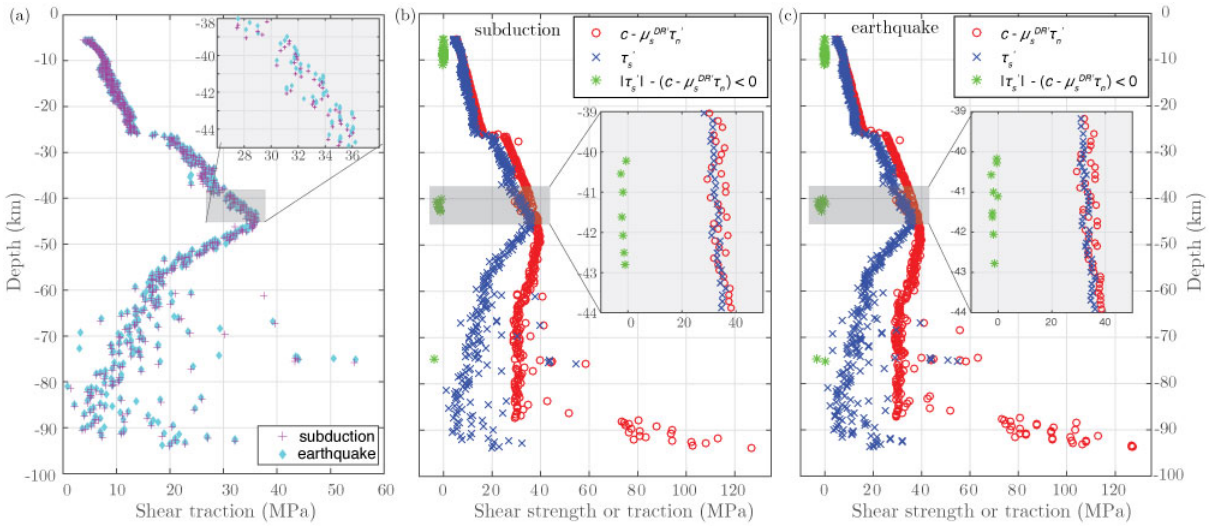

Figure A4. (a) Comparison between the effective shear traction, τ_s', on the faults in the subduction and earthquake models for the subduction-earthquake-tsunami test case. Failure analysis according to the earthquake model failure criterion (Eq. 1) at points along (b) the subduction model fault and (c) along a slice at $y = 0$ through the earthquake model fault. Variables are defined in text near Eq. 1. Values are before changes are made to c in the sediments and to μ_s at outliers, as discussed in the text.